3D characterization of individual grains of coexisting high-pressure H2O ice phases by time-domain Brillouin scattering

Sandeep Sathyan, Théo Thréard, Elton de Lima Savi, Nikolay Chigarev, Alain Bulou, Vincent Tournat, Andreas Zerr, Vitali Goussev, Samuel Raetz

3D characterization of individual grains of coexisting high-pressure H_2O ice phases by time-domain Brillouin scattering

Sathyan Sandeep,[1, a)] Théo Thréard,[1] Elton De Lima Savi,[1, a)] Nikolay Chigarev,[1] Alain Bulou,[2] Vincent Tournat,[1] Andreas Zerr,[3] Vitalyi E. Gusev,[1, b)] and Samuel Raetz[1, 4, c)]

[1)]*Laboratoire d'Acoustique de l'Université du Mans (LAUM), UMR 6613, Institut d'Acoustique - Graduate School (IA-GS), CNRS, Le Mans Université, France*

[2)]*Institut des Molécules et Matériaux du Mans (IMMM), UMR 6283, CNRS, Le Mans Université, France*

[3)]*Laboratoire de Sciences des Procédés et des Matériaux (LSPM-CNRS UPR-3407), Université Sorbonne Paris Nord (USPN), 93430 Villetaneuse, France*

[4)]*Associate member of Laboratoire Cogitamus, Av. O. Messiaen, 72085 Le Mans cedex 9, France*

(Dated: 2 July 2021)

Time-domain Brillouin scattering (TDBS) uses ultrashort laser pulses to (i) generate coherent acoustic pulses of picoseconds duration in a solid sample and (ii) follow their propagation in order to image material inhomogeneities with the axial resolution that can be deeply sub-optical, to nm-scale, and the lateral one down to the optical diffraction limit (half the optical wavelength of the probe laser). TDBS permits highly resolved 3D-imaging of grains in polycrystalline transparent samples with unlimited lateral sizes and thicknesses of at least 10 µm also when samples are orientationally textured and/or located in devices permitting access along one direction and from one side only. This optical technique presents, accordingly, clear advantages compared to any X-ray-based computed tomography (neither back-projection algorithm nor multiple viewpoints of the sample is needed) and classical spectroscopic methods. Here, we applied TDBS to the 3D-imaging of a sample of polycrystalline water ice containing two high-pressure phases. The imaging, accomplished via a simultaneous detection of quasi-longitudinal and quasi-shear waves, provided shape, coordinates, phase content and crystallographic orientation of resolved crystallites in a common coordinate system. Monitoring of acoustic pulses simultaneously propagating in two neighboring grains provided a new tool for the localisation of grain boundaries.

[a)] these authors contributed equally to this work
[b)] Electronic mail: vitali.goussev@univ-lemans.fr
[c)] Electronic mail: samuel.raetz@univ-lemans.fr

I. INTRODUCTION

High-resolution imaging of the state and evolution of texture, phase and/or chemical composition of polycrystalline solids upon any kind of action is a rapidly developing branch of scientific and industrial research, especially when texture strongly influences behavior and performance of the entire material or device. Examples of such devices or materials are electrodes of Li-ion batteries whose evolution upon charging/discharging may cause strong degradation of the battery capacity[1]; optoelectronic devices whose performance depends on homogeneity of the constituting material[2]; or rocks in the deep Earth where preferred orientations, shape, phase transitions, partial melting or change in distribution of the constituting minerals (mostly silicates and oxides) can initiate abrupt large-scale displacements leading to earthquakes[3].

Until now, the most elaborated way to examine texture of polycrystalline solids, with the spatial resolution similar or better than the grain sizes, is X-ray microscopy because this radiation propagates through and interacts with sample and thus reveals texture, chemical, electronic and/or structural inhomogeneities in its interior. In order to perform such characterization at µm- to nm-scale, dozens of X-ray-based approaches have been developed. They can be distinguished not only with respect to the principal mechanism of the signal generation but also with the technique used for the signal detection and/or imaging[2,4–6]. Most techniques provide two-dimensional projections of sample interiors which can be converted to three-dimensional (3D) images via computed tomography (CT) requiring collection of multiple projections upon rotation of samples by 360° and, accordingly, an unhindered sample accessibility along at least two spatial directions. These techniques impose limitations on the shape of the entire sample which should have comparable dimensions in all space directions and be preferably cylindrical. These two requirements are difficult to fulfill in examination of samples with a high aspect ratio, such as coatings on extended substrates or disk-shaped samples compressed to ultrahigh pressures in diamond anvil cells (DACs) where samples have typical dimensions of 50-400 µm in diameter and of 10-50 µm in thickness (*e.g.* in Refs. 7–9).

For examination of dense polycrystalline samples in general, but with a large diameter-to-height ratio or with a limited access in particular, a better solution than X-ray-based CT is to get local information, *i.e.* information from a limited volume in the sample usually named *voxel* (with sizes corresponding to the 3D-spatial resolution of the applied technique), directly from signals collected along a single direction. If such signals provide segmented information along

this direction, a 3D image corresponding to the juxtaposition of voxels can then be obtained by moving the probed limited volume (voxel) along two other perpendicular directions. Such opportunity/procedure is accessible via optical methods: strong focusing of laser light exciting Raman or classical frequency-domain Brillouin spectra permits extraction of 3D-resolved local information in the interior of transparent samples. However, in the absence of a control over the thermal phonons spatial localisation, the axial (*i.e.* along depth) resolution cannot be better than the Rayleigh distance of the focused radiation[10,11]. Thus, the dimensions of a voxel in that case are those of the 3D volume defined by the optical focal spot. Note that in our previous publication[12], most of the achievements in 2D- and 3D-imaging at high pressures, reported at that time and including X-ray-based techniques and frequency-domain Brillouin scattering, were already reviewed. While Raman spectroscopy is useful in only few special cases where samples contain compounds having distinct Raman spectra with strong lines, which is often not the case (e.g ice VI and VII, NaCl, MgO, $\mathrm{Al_2O_3}$, etc.), the classical frequency-domain Brillouin scattering (FDBS) can provide, in principle, an integral/holistic information on the state and texture of a polycrystalline transparent sample in 3D. This integral 3D information includes coordinates of each grain (if resolved) with respect to others–independently of their phase composition, the grain shapes, identification of the phase of particular grains, and crystallographic orientation of the identified grains with respect to a common coordinate system. Up to now, the record resolution, *i.e.* voxel dimensions, in FDBS has been reported in the confocal optical geometry: $\sim 0.5 \times 0.5 \times 2$ µm^3, yet at ambient conditions[10,11]. Using an oil-immersion objective lens, the resolution has even been recently enhanced[13] down to $\sim 0.3 \times 0.3 \times 1.1$ µm^3. However, maintaining such axial resolution by the application of the confocal optical FDBS microscopy for long working distances (around 10 mm or even more) is technically demanding, if ever possible. Examples of experiments, where such distances are inevitable, are examination of samples compressed to ultrahigh pressures in a DAC, heated in an oven, or cooled in a cryostat. In common FDBS experiments on samples compressed in a DAC (which is possible thanks to the transparency of diamond anvils that squeeze samples) and similar measurements requiring long working distances, the FDBS spectra are collected from the volume, whose axial dimension is controlled either by the sample thickness or by the light penetration depth. In both cases, the FDBS technique does not provide any depth-resolved information for samples having thicknesses between 10-50 µm, but provide information averaged along the complete thickness of the tested volume.

Another opto-acousto-optical technique, capable of providing down-to-nanometers axial res-

olution, and not dependent on the working distance of the focusing optical element, was used in the present work. It is based on the interaction of light with a propagating coherent density perturbation (an acoustic pulse) caused by coherent non-thermal acoustic phonons. The lateral resolution, *i.e.* the lateral dimensions of voxels, of this technique is the same as for any other optical method, down to about half the wavelength of the used probe light radiation. The technique had been pioneered for materials characterization at ambient conditions under the name of picosecond acoustic interferometry[14,15], while currently the names of time-resolved or time-domain Brillouin scattering (TDBS) have become more common[16]. In this technique, based on the principles of pump-probe time-resolved experiments, pump laser pulses of the picoseconds-femtoseconds duration launch coherent acoustic pulses (CAPs) of picosecond duration in a solid transparent sample via one of the possible mechanisms of optoacoustic conversion[17,18]. The probe laser pulses of picoseconds-femtoseconds duration, launched with adjustable time delays after the pump pulses, are used to follow in time the propagation of the CAPs thanks to the probe light scattering by the CAPs via opto-acoustic (photoelastic) effect[19,20]. As the light scattering takes place only in the volume occupied by a CAP, the axial spatial resolution of the TDBS technique along the path of the CAP, *i.e.* the dimension of voxels along the CAP propagation direction, can be deeply sub-optical because typical width of a 10 ps duration CAP is shorter than 40 nm[16,21–23] and further shortens with diminishing duration of coherent acoustic pulses or of the strain gradient fronts inside them[16]. Thus, the axial resolution of the TDBS technique can outperform that of the FDBS microscopy, independently of the working distance between the sample and the objective lens used to focus the pump and probe beams and to collect the scattered light. Application of the TDBS depth-profiling and imaging therefore provides opportunities and advantages earlier unavailable in the solid state research where the long working distances are inevitable. Examination of samples compressed to ultrahigh pressures in a DAC is one of such cases we are dealing with below. The TDBS approach was introduced into high-pressure research quite recently[24,25]. It was applied for the depth-profiling of polycrystalline water ice and solid argon up to Megabar pressures[12,26], revealing, in these densified granular assemblages, not only μm-sized textures at the sample surface as one could get using other approaches but also, and for the first time, sub-μm- and μm-sized inhomogeneities along the sample axis, currently inaccessible in a DAC when using the FDBS technique as well as for the X-ray-based techniques. The TDBS technique was then applied for the measurement of pressure-dependencies of single crystal elastic moduli of cubic H_2O-ice[27] and solid argon[28], with a demonstrated better precision than by FDBS.

Although the above-mentioned experimental approaches[12,26–28] have already demonstrated efficiency of the 2D TDBS-based imaging for qualitative and quantitative characterization of materials elasticity and phase transitions, they were not sufficient for visualisation and examination of texture and its evolution in time, upon compression or any other action on a difficult-to-access sample (*e.g.* in an oven or a cryostat). To do so, 3D imaging of sample inhomogeneities is required. The 3D TDBS imaging has been first realised at ambient conditions in animal and biological cells[29,30], which are weakly inhomogeneous objects where regions having distinct elastic and/or optical parameters are separated by curved interfaces[29–31]. At ambient conditions, TDBS experiments on polycrystalline materials with large grain sizes were already reported, and it was found that the TDBS imaging inside individual grains is straightforward[32–36]. In particular, simultaneous monitoring of the propagation of quasi-longitudinal acoustic (LA) and quasi-transverse acoustic (TA) pulses inside a grain by TDBS was demonstrated[32,33]. Taking advantage of this feature, the TDBS technique provided opportunity to determine the orientation of an individual grain boundary in 2D geometry[34]. The first step to the 3D imaging of polycrystalline materials at ambient conditions was undertaken in the recent work of Wang et al.[35] where the boundary between two adjacent grains and their relative crystallographic orientations were reconstructed in 3D space using the simultaneous TDBS imaging with LA and TA pulses. However, an integral/holistic 3D imaging of a polycrystalline sample (*e.g.*, H_2O ice) containing, in addition to multiple grains, two different high-pressure phases (ice VI and ice VII) is here performed and presented for the first time. This particular case of a sample compressed in a DAC should be considered by the reader as an example of experiments with a sample inside a relatively heavy device providing access from only one side, which excludes the possibility to use X-ray-based approaches as well as the classical spectroscopic techniques for the high-resolution 3D imaging.

Extending several concepts developed recently in the TDBS experiments at ambient conditions, we succeeded to generate an integral 3D image of a polycrystalline sample in a DAC containing multiple differently oriented grains of two high-pressure phases of H_2O ice. We were able to determine the position and shapes of grains constituting the sample in the complete $\sim 100 \times 100 \times 10$ μm^3 volume with the lateral resolution of 2.5 μm and the axial resolution of 1.2 μm as well as orientation of their crystallographic axes with respect to a common system of coordinates. First experimental observation of coherent TA pulses in TDBS measurements at high pressures was crucial in obtaining the orientation of crystallographic axes of individual ice grains. Combining this observations with the signals generated by LA pulses, we could distinguish grains

of H_2O ice VI from those of H_2O ice VII coexisting at the pressure of our experiment, 2.15 GPa. In addition, we report on observation of particular TDBS signals, corresponding to the propagation of LA pulses in two neighbor grains simultaneously, which provides an original opportunity to localize boundaries between grains. The main prerequisite of such experiments is the earlier determined densities, refractive indices and single crystal elastic moduli of both H_2O-ice phases. In our opinion, 3D images collected using the TDBS-based approach can be considered as standards for verification of the reliability of back-projection models used in the X-ray-based CT. This is because the 3D TDBS images are directly obtained from spatially 3D-resolved data requiring a minimal level of assumptions, as described below.

II. SAMPLE PREPARATION AND EXPERIMENTAL SET-UP

A. DAC and the sample

The high-pressure experiments on water ice were performed using a diamond anvil cell (DAC) of the Merrill-Bassett type[37]. We used diamond anvils with unbevelled culets having a diameter of $\sim$ 500 µm. A hole of $\sim$ 180 µm in diameter drilled in the center of a stainless steel gasket pre-indented to the thickness of $\sim$ 60 µm represented the sample volume [Fig. 1(c)]. The latter was filled with bi-distilled water that solidified upon compression. The sample volume contained also a thin iron disk and few ruby grains of 1-5 µm in size distributed in the space between the iron disk and the gasket wall. The iron disk served as the opto-acoustic generator for launching coherent acoustic pulses into the ice sample. It was obtained by a gentle compression of a small iron spherule between the diamond anvils, whose surfaces are parallel to each other, until the desired thickness was obtained. The disk was initially in contact with one of the anvils but lifted up on one side by a few microns when the sample volume was filled with water [Fig. 1(c)]. Note that the shape and the orientation of the iron generator presented in Fig. 1(c) are illustrative. The ruby grains were used to measure pressure using the calibrated shift of the R1 fluorescence line with compression[38]. Finally, the H_2O ice sample was compressed to 2.15 GPa until the ice VI and ice VII phases were simultaneously present in the sample volume. The ruby fluorescence spectra were collected with an Ocean Optics USB4000 spectrometer. Within the instrument resolution, the pressure was found to be the same in all points around the sample. The collected spectra were fitted with the Gaussian-Lorentzian function to obtain position of the R1-line maximum. Corre-

sponding pressure was calculated to be 2.15 ± 0.05 GPa using the calibration for quasihydrostatic load conditions[38].

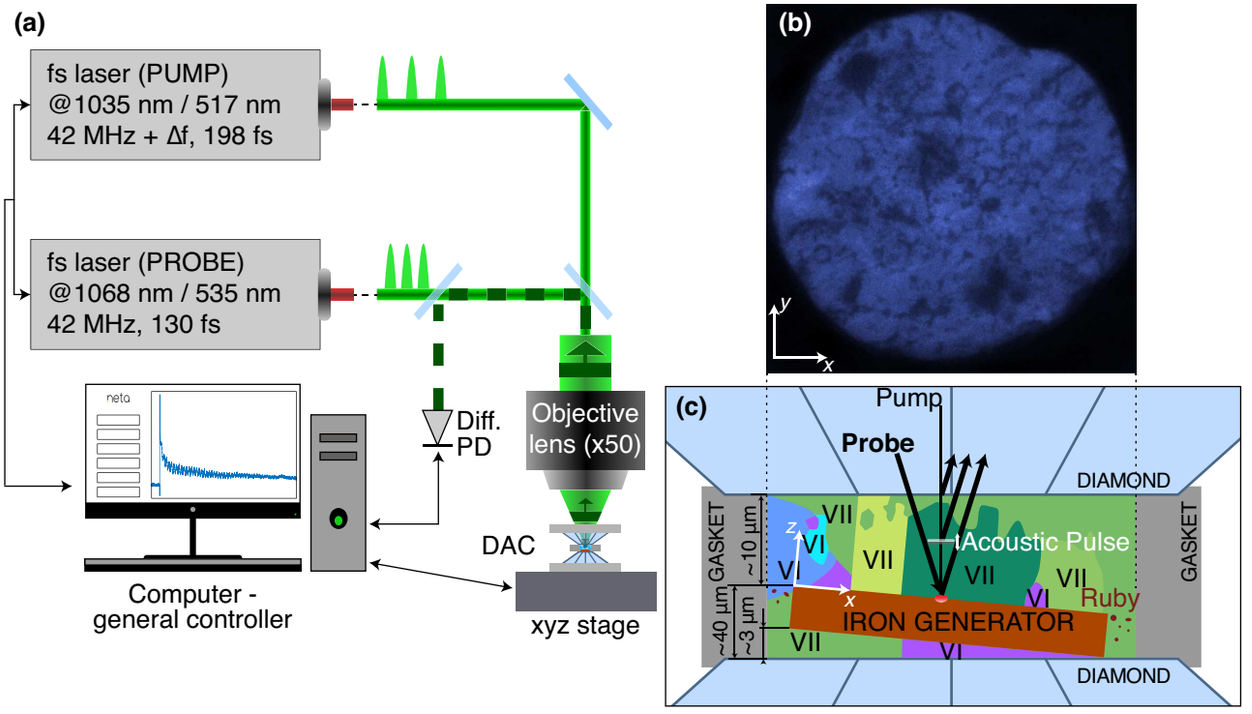

FIG. 1. (a) Experimental set-up of the picosecond acoustic microscope (JAX-M1, NETA, France) and (b) optical image of the H_2O ice polycrystal in the DAC between the diamond anvil and the iron optoacoustic transducer. (c) Magnified cross-sectional side view of the DAC. The results of the TDBS experiments (see Figs. 3 and 4) revealed the coexistence in the sample of two phases, ice VI (bluish) and ice VII (greenish). The disk-shape iron opto-acoustic generator inside the sample chamber has the diameter of about 100 µm. It touches the lower diamond anvil at its right end. Even though the pump and probe laser paths are collinear in the experiment, the probe one is shown inclined for a better visualisation of its different reflections. The coordinate system used below is shown by white arrows in (b) and (c).

B. Pump/probe ASOPS set-up

The experimental set-up is a commercial picosecond acoustic microscope (JAX-M1, NETA, France)[39] based on asynchronous optical sampling (ASOPS) with pump and probe laser beams following the same path within the DAC, as shown schematically in Fig. 1(a). Two pulsed fiber lasers of optical wavelength of 1034.8 nm and 1068.4 nm, of pulse duration 198 fs and 130 fs, respectively, and with a repetition rate of 42 MHz are synchronised for asynchronous optical sampling[40]. The repetition rate of the follower laser cavity is slightly offset compared to that of the leader one. The used offset in our measurements of 500 Hz corresponds to a temporal sam-

pling of 0.28 ps. The two optical wavelengths obtained by frequency doubling of the fundamental radiations, 517 nm and 535 nm, were used as pump (follower cavity) and probe (leader cavity), respectively. The beams were normally incident and co-focused on the surface of the iron disk to the spot of approximately 1.25 µm radius at the $1/e^2$ level of the laser intensity. The averaged power of the pump laser was 7 mW and that of the probe laser 13 mW. Note that the chosen beam powers have been set to maximize the ratio of the useful signal over noise: the probe power is nearly twice that of the pump in order to have a large enough reference and scattered probe light reaching the photodetector, which allows diminishing the number of averages and hence the overall time of the experiment. The sample analysed in this work was a water ice polycrystal compressed in a DAC to a pressure of 2.15 GPa, as presented in the previous section, with an embedded iron optoacoustic transducer for launching the CAPs[41]. The optical image of the H_2O ice polycrystal in the DAC shown in Fig. 1(b) reveals some dark areas on the iron transducer corresponding to low local optical reflectivity of iron, that could be due to some degradation processes[41]. For the imaging experiments, the sample was mounted on a X-Y positioning stage equipped with step motors ensuring the positioning precision of 0.16 µm. For the below-presented images, the step was 1.25 µm along x- and y-axes [see Fig. 1(b)-(c) for the coordinate system]. As shown in Fig. 1(c), the origin of the z-axis is at the surface of the iron transducer.

III. RESULTS

A. Typical experimental signals

In the TDBS experiments, the probe light scattered by moving CAPs and the probe light reflected by various stationary optical inhomogeneities of the sample interfere on a photodetector surface and thus produce a signal oscillating in time. In the considered experiments, the most important stationary sources of the probe light reflection are (i) the metallic optoacoustic transducer where the pump and probe laser pulses are co-focused and (ii) the interface between the diamond anvil—providing optical access to the compressed sample—and the water ice [see Fig. 1(c)]. Heterodyne detection in the TDBS technique is essentially interferometric and sensitive to the relative phase of the acoustically scattered and reflected probe light[14,15]. Because of a CAP propagation at its mode velocity, the phase of the light scattered by this CAP is continuously varying in time. The TDBS signal, due to the interferences on the photodetector of the acoustically-scattered probe

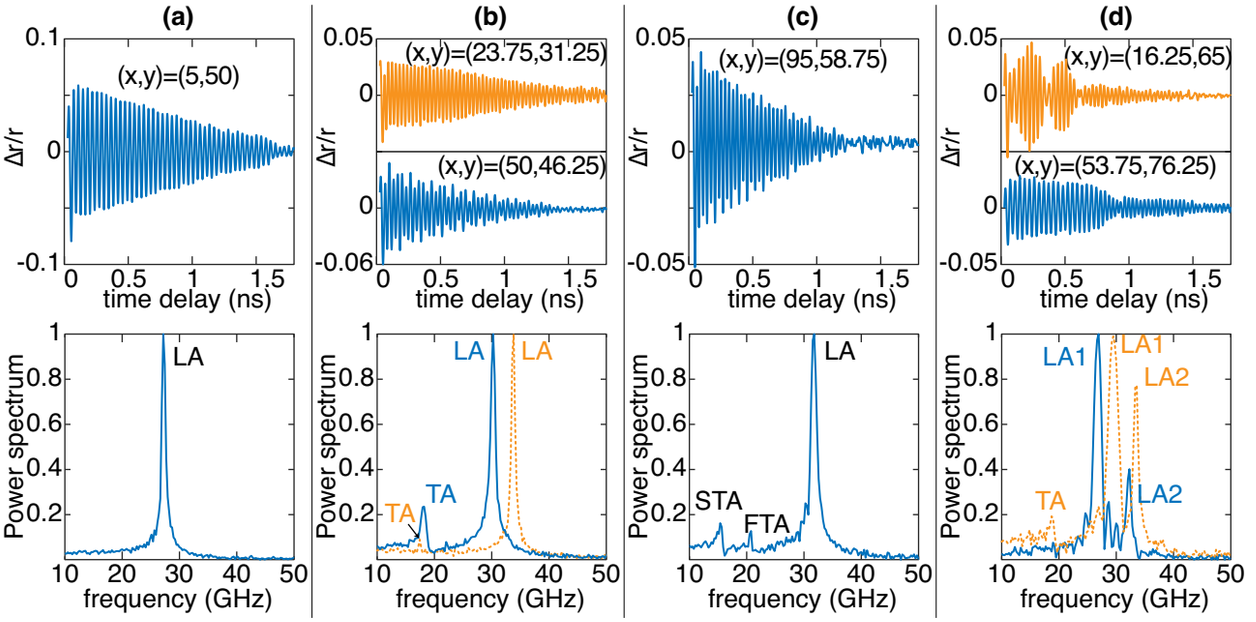

FIG. 2. Experimental acoustic contributions to transient reflectivity signals as a function of time delay (upper row) and their Fourier spectrum density (lower row) in four typical cases: (a) a single quasi-longitudinal acoustic (LA) mode, (b) a LA and one quasi-transverse acoustic (TA) modes with low (orange lines) and large (blue lines) relative shear amplitudes, (c) a LA and two TA modes, and (d) two LA modes propagating in two different grains "in parallel" (orange lines) and "in sequence" (blue lines). The coordinates x and y of the measurement points, which are indicated in the first row, correspond to the positioning (in µm) of the ice sample in the coordinate system presented in Figs. 3 and 4.

light and the reflected one, is oscillating with extrema and zeros corresponding to the constructive and destructive interferences, respectively. The oscillating TDBS signal, commonly called the Brillouin oscillation (BO), contains the delay-time dependent information about variations of optical, elastic, and photo-elastic properties in the sample along the CAPs propagation direction which can be converted to the length/depth scale. The typical oscillating TDBS signals, obtained for different lateral positions on the imaged area of the water ice sample, are presented in the first row of Fig. 2. These signals are obtained from the raw transient reflectivity signals captured by a photodetector followed by filtering, subtracting the thermal background and cutting of initial peaks generally observed at the instants when the pump and probe laser pulses overlapped. First the signal is filtered with a 48th-order FIR bandpass filter with passband $10 < f < 50$ GHz according to the expected Brillouin frequencies from Tab. I. Then, the remaining-after-filtering background was subtracted applying the local regression method LOESS from Matlab® using weighted linear least squares and a 2nd degree polynomial model[42] with 319 points of span of the moving average (*i.e.*, the window span for the moving average is about 0.15 ns). Because the fast non-oscillating

transients of optical reflectivity near the initial time are difficult to remove without influencing the high-frequency Brillouin oscillations (Brillouin peak), the first 25 ps of the remaining signal were cut. Therefore, the first tens of nanometres next to the iron generator are lost for the analyses. We applied a similar treatment to all signals presented in this paper before further processing.

The characteristic frequencies of the BOs in the TDBS signal (see Fig. 2) correspond to the frequencies of the Stokes/anti-Stokes frequency shifts of the scattered light in the FDBS technique, *i.e.*, to the Brillouin frequency (BF)[19,20]. In our experimental geometry, where the coherent CAPs and the probe light are propagating collinearly, the most efficient process of the photon-phonon interaction is the backward scattering of the probe light. In this case, the BFs ($f_{B,\alpha}$) are related to the velocities (v_α) of the coherent acoustic phonons, where α stands for the type of the acoustic mode (LA or one of the TA), by the following relation:

$$f_{B,\alpha} = \frac{2nv_\alpha}{\lambda_{\text{probe}}}, \tag{1}$$

where n is the refractive index of the transparent media at the wavelength in vacuum λ_{probe} of the probe laser pulses. The Fourier analysis of the BOs is therefore commonly the first step used to reveal the physical origins of variations of BF of each of the TDBS signals.

Fourier spectra of typical BOs detected in our sample are presented in the second row of Fig. 2. These spectra clearly indicate that the TDBS signals have contributions from different types of the CAPs in the different lateral positions of our sample. This was used in the following for 3D TDBS imaging. Near the pressure of 2.15 GPa, corresponding to the transition at room temperature from the lower-pressure phase VI to the higher-pressure phase VII of H_2O ice[41], the available data on the optical and elastic properties (see Table I) provide the opportunity to estimate the expected BFs in both phases of ice (see Appendix for detailed explanations of these estimations and their uncertainties). The comparison of the spectra presented in Fig. 2 with the results of these estimations, presented in the last row of Table I,indicated that not only LA modes but also TA modes are contributing to our detected TDBS signals. The latter is observed for the first time in high-pressure TDBS experiments. The BOs presented in Fig. 2(a)-(c) can be attributed to the Brillouin scattering by a single LA mode, by a LA and one TA modes, and by a LA and two TA modes, *i.e.* fast (FTA) and slow (STA), respectively. It is worth noting here that, potentially, in optically anisotropic ices, a single acoustic mode could produce up to three different BFs because of the birefringence phenomena giving rise to BS with optical mode conversion[32,33]. However,

Phases of H_2O ice (*Lattice system*)		**VI** (*Tetragonal*)	**VII** (*Cubic*)
Density[43,44] ($g\,cm^{-3}$)		$\rho = 1.419$	$\rho = 1.600$
Elastic constants[44,*] (GPa)		$C_{11} = 40.56$ $C_{12} = 13.75$ $C_{13} = 18.59$ $C_{33} = 34.43$ $C_{44} = 7.50$ $C_{66} = 6.39$	$C_{11} = 37.61$ $C_{12} = 19.17$ $C_{44} = 21.59$
Refractive index @ 515 nm[43,44]		$n = 1.468$	$n = 1.521$
Brillouin frequency range (GHz)	LA: FTA: STA:	$[26.71 - 29.37]$ $[12.63 - 16.89]$ $[11.66 - 12.80]$	$[27.58 - 33.09]$ $[16.46 - 20.90]$ $[13.66 - 20.90]$

[*] Our TDBS results for ice VII[27] agree reasonably well with those reported in Ref. 44

TABLE I. Properties of the high-pressure phases VI and VII of H_2O ice near the pressure of 2.15 GPa and used to calculate the ranges of BFs for the LA, the fast TA (FTA) and the slow TA (STA) modes. The uncertainties in the estimated ranges of the Brillouin frequencies of different acoustic modes are discussed in the appendix.

the phase VII of H_2O ice is cubic (and thus optically isotropic), while the birefringence of the hexagonal phase VI is too weak (less than 1%[43]) to be observed in our TDBS experiments.

The beating in the BO evidenced in Fig. 2(d) demonstrates that the LA pulses are propagating in two differently-oriented grains of ice. The orange lines correspond to their propagation in both grains simultaneously, *i.e.* "in parallel". On the contrary, the blue lines correspond to the case when the LA pulses are propagating first in one grain and then in another one, *i.e.* "in sequence". The BOs corresponding to the sequential TDBS in two different media, *i.e.* the TDBS imaging of the LA CAP transmission from one medium into another were already reported multiple times, for example for ice/diamond interface[12], for the interface between ice VII and ice VI[41] and for SiO_2/Si interface[45,46]. The sequential propagation of the LA CAPs in two different grains of a polycrystal was reported as well[34]. Note that there are also some reported observations of the simultaneous monitoring in two different media of two different LA CAPs propagating in the opposite directions: for example, the CAPs transmitted through and reflected from the interface between two media[45]. Here however, we report for the first time the TDBS monitoring of two LA CAPs propagating in parallel and in the same direction in two differently oriented ice grains along

their mutual interface. In the next subsection, it is revealed that all the TDBS signals of the type, highlighted in Fig. 2(d) with the orange colour, are detected in the vicinity of grain boundaries and are never detected in the grain volume. The latter suggests that the detection of these kind of TDBS signals could be fruitful for a fast localisation of grain boundaries, *in situ* and in real time.

B. 2D TDBS projections obtained with LA and TA coherent acoustic pulses and grain identification

The 2D TDBS projections in Fig. 3 highlight the contribution of the most prominent grains with a particular velocity of (a) LA mode or (b) one of the TA modes related to the orientation of those grains. The color maps in Fig. 3 represent indeed the dominant frequency content attributed to (a) LA modes and (b) TA modes of the first two nanoseconds of the TDBS signals observed in the polycrystalline ice sample covering a round disk-shaped iron optoacoustic transducer of about 50 µm radius [Fig. 1(b,c)]. The chosen time interval corresponds to the acoustic propagation time through about 10 µm of the ice sample at a LA mode velocity. The TDBS signals are not observed in the locations indicated by white pixels due to poor signal-to-noise ratio. Note that the white pixel areas in Fig. 3(a) match the dark tones in the optical image of the sample [Fig. 1(b)]. It is important to note that while individual crystallites in the sample are not visible on the optical image, their presence is obvious in the 2D TDBS projection.

The black open squares in Fig. 3(a) depict pixels where a beating phenomenon of the kind "in parallel" (orange) in Fig. 2(d) has been observed. The automatic gathering of those pixels has been performed by tracking the signals that have two peaks in the spectrum density within the LA frequency range and that show at the same time a peak at the difference frequency in the spectrum density of its envelope. It is clearly visible from Fig. 3(a) that such signals are only found in locations in the vicinity of grain boundaries and never in a grain volume. We propose that this feature can be used for grain boundary imaging (see Discussion).

To obtain the map of TA modes [(Fig. 3(b)], we have extracted prominent frequency peaks in the 10 to 22 GHz frequency range, which excludes the LA modes (see Table I). The TA map is less complete than the LA one because TA modes have usually lower amplitudes in TDBS signals than LA modes, making them more difficult to detect/observe. Nevertheless, even TA modes with weak amplitudes are detected in the data with good signal-to-noise ratio as shown by the dashed orange curve of the spectrum density in Fig. 2(b). The white solid lines in Fig. 3(a) indicate areas where

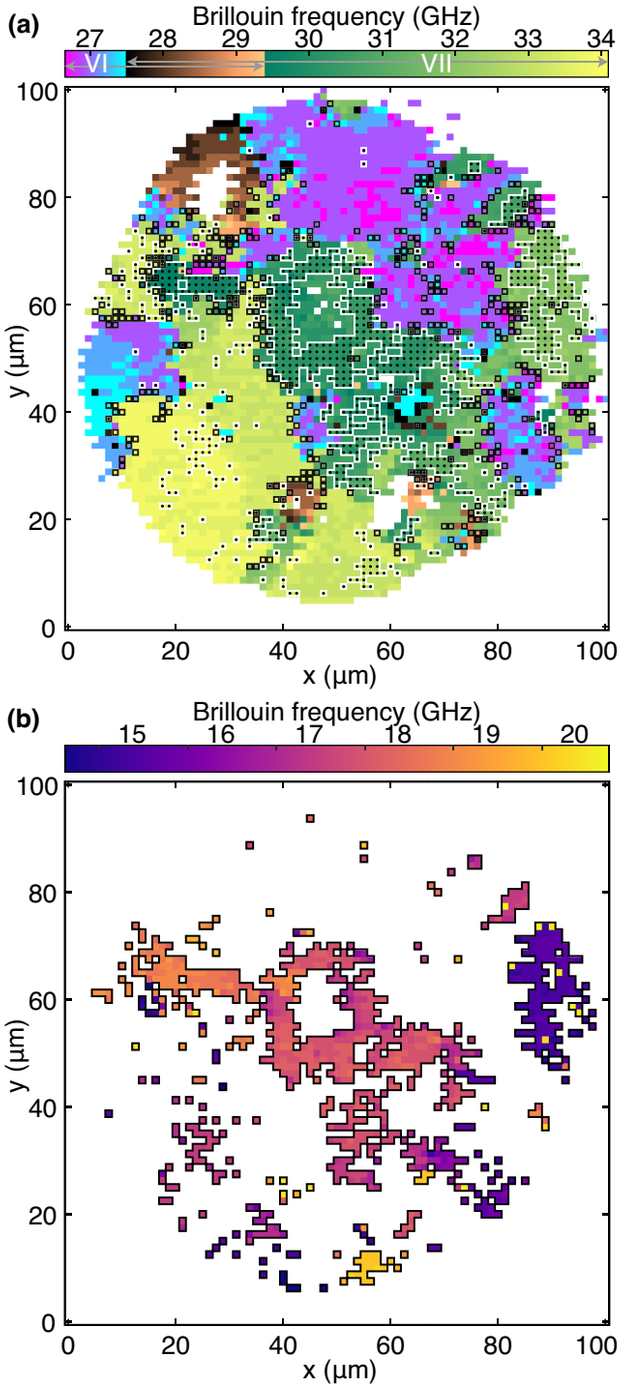

FIG. 3. Dominant frequency content attributed to (a) LA modes and (b) TA modes of the first two nanoseconds of the TDBS signals observed in the 100×100 μm^2 area of the ice sample. The white solid lines in part (a) delimit areas where the TA modes shown in (b) have been detected. In (a), each pixel shown in (b) is marked with a central black dot. The black open square markers show the pixels where a beating phenomenon of the kind presented by the top (orange) signal in Fig. 2(d) has been observed.

the TA modes shown in Fig. 3(b) have been detected. Each pixel shown in Fig. 3(b) is marked

with a central black dot in Fig. 3(a). It is interesting to note that most of the detected TA modes are recorded in the voxels where the frequency content is higher than 29.4 GHz (greenish color scale), showing that the TA modes with decent amplitudes are all found in the phase VII of H_2O ice, and mainly where the LA velocity is rather low (dark green) or high (light green). The lowest part of the color bar in Fig. 3(a), where the frequencies lower than 27.5 GHz are (magenta-to-cyan color scale), depicts the crystallites belonging to the phase VI of H_2O ice. Interestingly, almost no TA modes are detected in these specific locations of the sample, which suggests that the monitoring of TA modes in the phase VI is, for the present state of the technique, very unlikely, not to say impossible (see next section). Note that in the center-right grain (around $x \approx 90$ µm and $y \approx 60$ µm) in Fig. 3(b) with the lowest TA frequencies, the color of some neighboring pixels is occasionally switching from dark violet, *i.e.* the lowest frequency of the color scale, to light yellow, *i.e.* the highest frequency of the color scale. This is because the figure represents the dominant frequency content in the TA frequency ranges and this particular grain contains two detectable TA modes. The amplitude of the slow (S) TA mode is usually higher than that of the fast (F) TA mode, except in some (light yellow) locations. The area where identification of the main ice phase remains unclear from the first analysis of the dominant frequency content of the LA signals, *i.e.*, where the frequency is greater than or equal to 27.5 GHz and lower than or equal to 29.4 GHz are depicted in a copper color in the scale in Fig. 3(a).

C. 3D TDBS imaging with LA coherent acoustic pulses

In order to obtain 3D images of the sample texture using the collected TDBS signals, we used a usual short-time Fourier transform. Fig. 4 represents the depth-resolved information of the ice sample texture recovered using the LA mode. Although the same imaging with TA coherent acoustic pulses is possible, the detected TA modes are too sparse [see Fig.3(b)] to obtain an informative 3D image. The latter is explained by very low power of both pump and probe lasers needed to preclude the non-thermal transformation of ice VII into ice VI (see below).

In Fig. 4, we estimate the dominant LA-mode-related frequency at different depths by calculating the FFT of the acoustic signal sliced with a Hann window of 0.23 ns (about 7 oscillations of the LA mode), which gives an axial resolution of about 1.2 µm. Using the temporal indication of the centre of the sliding window and the measured local velocities at the previous instants for the same acoustic mode, the time axis was transformed in the depth axis; the smaller the time, the

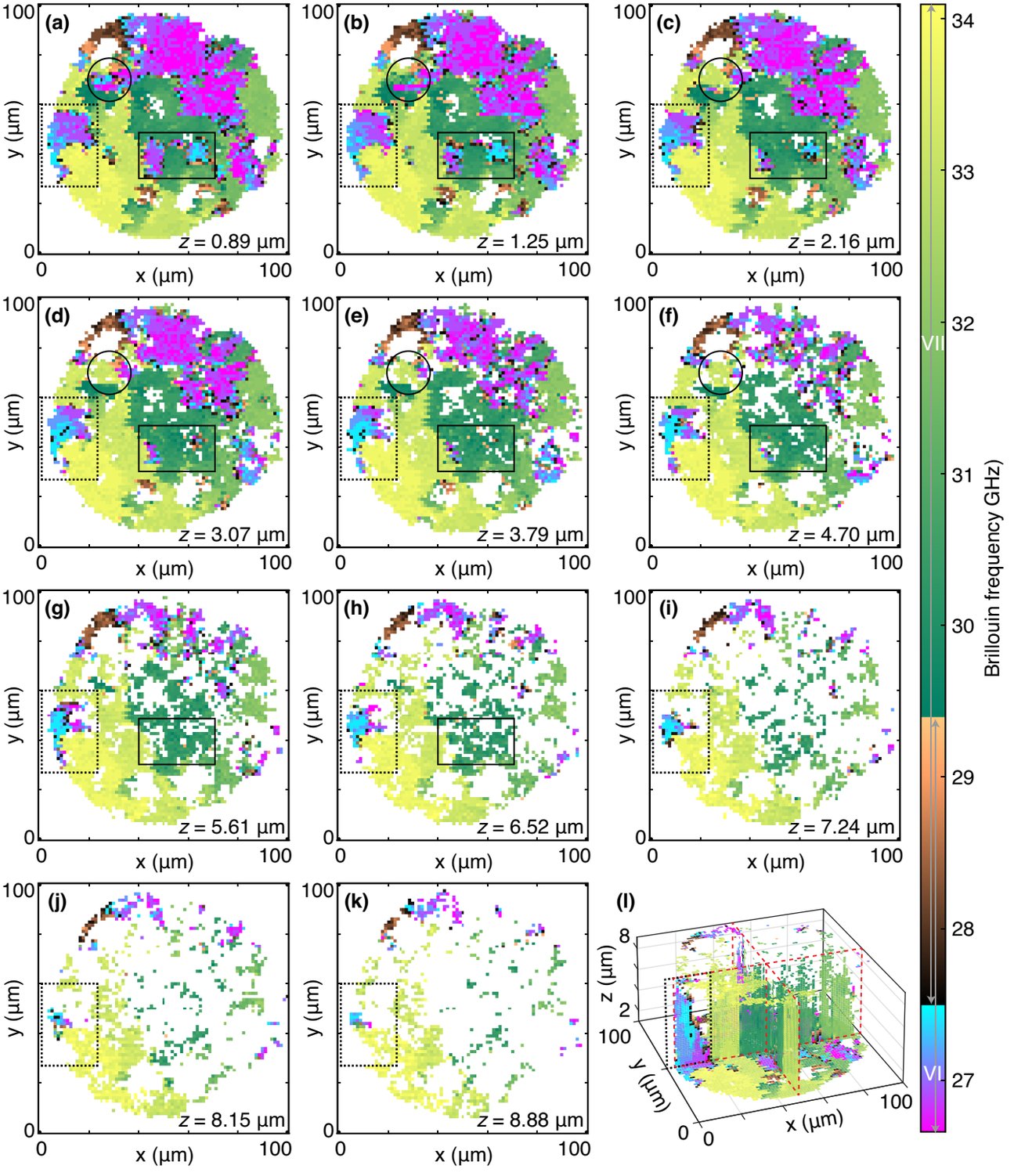

FIG. 4. 3D TDBS imaging of the polycrystalline H_2O ice sample. (a)-(k) The slices are shown at particular positions along the z-axis indicated in the right-bottom corner of each slice. In (a)-(f), the circles depict a volume zone composed of multiple small crystallites. In (a)-(h), the solid lines rectangles depict the zones where crystallites of the phase VI are seen between the optoacoustic transducer and the higher-located crystallites of the phase VII. In (a)-(l), the dotted lines rectangles depict zones with oblique boundaries between several crystallites of phase VI. (l) 3D representation of the complete probed volume with the first and last slices, (a) and (k) (xy planes), and the middle slices (yz and xz planes) at $x = 50$ µm and $y = 50$ µm, respectively (red dashed rectangles). The color map is common for all parts of Fig. 4 and is the same as in Fig. 3(a). It is important to note that for the sake of visibility of 3D textures, the vertical z-axis is expanded by 4 times when compared with the x- and y-axes.

closer the probed voxel to the iron optoacoustic transducer. Note that this change of coordinates implies knowledge of the local refractive index. For the sake of simplicity, we have chosen here to attribute only one refractive index to a given pixel, even when it contains two phases. The attribution of the refractive index is based on the previous determination of the phases of each grain as discussed in Fig. 3(a). This means that we used the refractive index of the dominant phase. We are aware that this will engender some distortions of the grains, which we consider as minor in this analysis. For pixels with unattributed phases ($f_{B,\mathrm{LA}} \in [27.5, 29.4]$ GHz), the refractive index is chosen to be the average of that of phases VI and VII. The resulting 3D-imaging is shown in Fig. 4 where each panel, except the last one (l), is a slice of the polycrystalline H_2O ice sample at a particular coordinate along the z-axis given in the right-bottom corner of each panel. In Fig. 4(l), a 3D representation of the complete probed volume is shown with the first and last slices, (a) and (k) (xy planes), and the vertical slices through the sample middle (yz and xz planes) at $x = 50$ µm and $y = 50$ µm, respectively (red dashed rectangles). The rectangles (shown with solid and dotted lines) and the circle mark in Fig. 4 indicate the sample regions/volumes with some interesting changes in the bulk revealed by this 3D imaging that are discussed in the following.

From the analysis of the 2D projection in Fig. 3(a), the volume zone pointed out by the circle in Fig. 4(a)-(f) is expected to be composed of multiple small crystallites because it contains numerous TDBS signals with beatings. It can indeed be seen in Fig. 4 that close to the iron optoacoustic transducer, this zone is made of multiple and relatively small crystallites depicted by different colors. About half of the voxels within the circle depicted in the slice at $z = 0.89$ µm (Fig. 4(a)) belong to ice VI crystallites. In the next slice at $z = 1.25$ µm, Fig. 4(b), it can be seen that in the place of the crystallites of phase VI with high LA velocity for that phase (cyan voxels, $f \approx 27.5$ GHz) the ice phase is now VII with low LA velocity for that phase (green voxels, $f \approx 31.1$ GHz). From that slice to the next one at $z = 2.16$ µm, Fig. 4(c), the voxel color slightly changes to lighter green, which could be temptatively attributed to a change from one phase VII crystallite to another having a deviating crystallographic orientation. Yet, the resolution along z of about 1.2 µm controlled by the width of the Hann window means that the frequency/color attributed to those voxels in the slice in Fig. 4(b) is indeed a weighted average of the frequency of the phase VI crystallite (close to the transducer) and that of the phase VII [higher in the DAC, see Fig. 1(c) for illustration]. An even more precise depth localisation of the boundary between the two could be done but requires a more sophisticated signal processing. The rectangles shown by solid lines [Fig. 4(a)-(h)] depict also the zones where crystallites of the phase VI are seen between

the optoacoustic transducer and the higher-located crystallites of the phase VII. Interestingly, the frequency (and color in Fig. 4) is not switching here from that of phase VI to that of phase VII at the same depth for all pixels. This is the clear sign of an oblique interface between the two grains composed of different phases of H_2O ice. Last but not least, rectangles shown with dotted lines [Fig. 4(a)-(l)] surround other textural features demonstrating the 3D imaging capability of the TDBS technique. In this case, oblique boundaries between several crystallites of phase VI having different crystallographic orientations extend up to the ice/diamond interface. In Fig. 4(l), the inclined boundaries are clearly visible in the vertical slice (xz plane) at $y = 50$ μm.

IV. DISCUSSION

A. On the TDBS depth spatial resolution

In the 3D TDBS-ASOPS image shown in Fig. 4, shapes and coordinates of grains of both H_2O ice phases, obtained using the LA modes only, were measured with the spatial resolution similar to that achieved in the most recent XRD-based CT measurements[47,48]. In our work, the axial resolution was 1.2 μm and the lateral one, defined by focusing of the laser beams to be 2.5 μm, was approximately twice larger than the lateral step of the scans. The XRD-based CT permits reconstruction of 3D-images of texture-free or weakly textured samples with the stated spatial resolution of 1 μm. However, the technically possible spatial resolution of the TDBS-ASOPS method is much higher[16,31]. The lateral resolution, limited by the wavelength of the used lasers, can be improved to half the probe optical wavelength, down to 150 nm if UV-blue light lasers are used. The axial resolution of < 170 nm with our probe laser can be achieved if both LA mode and TA modes are used because it is only limited by the probed acoustic wavelength $\lambda_B = \frac{\lambda_{probe}}{2n}$. In our present 3D imaging, the axial resolution was controlled by the application of the time-frequency analysis technique known as the short-time Fourier transform requiring a balance between the frequency- and temporal (and thus axial) resolution. We had to keep the frequency resolution, which permits recognizing of grains having different crystallographic orientation, high enough to be able to differentiate frequency changes in the interval of the LA Brillouin frequencies of phase VI spanning only over 2.7 GHz (see Table I and Fig. 4). For this reason, the temporal size of the Hann window was 0.23 ns, which is theoretically even a bit small since the 3 dB bandwidth of such a window function is 3.2 GHz. In addition, one should not forget that a polycrystalline

aggregate under pressure in a DAC is usually subjected to stress inhomogeneity/nonhydrostaticity, which could lead to an induced optical anisotropy within the DAC and therefore could influence the obtained 3D images if not accounted for. This effect in our case is negligible. Indeed, we estimated a uniaxial stress component parallel to the load axis of the DAC of 30 MPa, from the measured 0.15 GPa difference in pressure between the center and the edge of the sample. In the case where the uniaxial stress component was estimated to be 1 GPa for a 4 GPa difference in pressure over 45 µm, we have already reported that the induced optical anisotropy in that case is negligible[12].

B. On the TDBS depth of imaging

The TDBS imaging theoretically allows imaging of transparent samples to the depths exceeding 100 µm but it can be limited by several factors such as (i) the coherence length of the probe laser pulses, $L_{\text{coherence}}^{\text{probe}}$, in the medium under evaluation, (ii) the diffraction length, L_R, of the probe laser radiation and of the coherent acoustic waves, as well as (iii) by the absorption of the acoustic pulses and probe light. For further details on depth of the TDBS imaging, we refer interested readers to the review article on advances in applications of TDBS for nanoscale imaging (Ref. 16) and references cited therein. We estimated the coherence length in our measurements using the equation $L_{\text{coherence}}^{\text{probe}} \equiv c_0 \tau_{\text{probe}}/(2n) \approx 15$ µm, where c_0 denotes the speed of light in vacuum, $\tau_{\text{probe}} \approx 150$ fs the duration of the laser pulses of our TDBS-ASOPS set-up, and $n \approx 1.5$ the refractive index of ice at $P = 2.15$ GPa for $\lambda = 515$ nm[43,44] (close to our probe wavelength $\lambda_{\text{probe}} \cong 535$ nm). The main limiting parameter was, obviously, τ_{probe} because, currently, only for this type of lasers (*i.e.*, fs lasers) the needed cavities synchronisation of the pump and probe lasers for ASOPS is available. Because of the strict relation between λ_{probe} in the medium and the wavelength of the coherent acoustic phonon at the Brillouin frequency, *i.e.* $\lambda_{\text{B}} = \frac{\lambda_{\text{probe}}}{2n}$, the Rayleigh range (*i.e.*, the diffraction length) of both the probe light beam and the coherent acoustic beam at Brillouin frequency, can be described by the formula: $L_R \equiv \frac{\pi a^2}{(\lambda_{\text{probe}}/n)}$, where a is the radius at $1/e^2$ level of the intensity distribution in the probe or in the pump laser beams. Because focusing of the pump laser beam controls the radius of the photo-generated CAPs and the pump and probe laser beams were co-focused, in our experiments, to the same spot with $a \approx 1.25$ µm, we obtained $L_R \approx 14.3$ µm, very similar to $L_{\text{coherence}}^{\text{probe}}$. However, the signal amplitude drops by e^2 times at the coherence length, while it decreases by only $\sqrt{2}$ times at the Rayleigh range. Accordingly, the influence of the diffraction

($\sim 1/[1+(v_{\mathrm{LA}}t/L_R)^2]^{1/2}$) on the depth of imaging was negligible in our experiments. We have confirmed this consideration experimentally. In some lateral positions, the gaps between the optoacoustic transducer and the diamond anvil were filled by single crystals as followed from the observed Brillouin oscillations within the complete gaps (see Fig. 1(c) and Supplementary information). In one of these positions, the quasi-longitudinal acoustic wave with $f_B = 26.85$ GHz and $v_{\mathrm{LA}} \approx 4881$ m s^{-1} propagated from the optoacoustic transducer to the diamond anvil in 2.15 ns, thus providing the distance of 10.5 μm. We note that, during the propagation, the Brillouin oscillation amplitude decreased by only 75%. We fitted the observed Brillouin amplitude decay by accounting for (i) the Gaussian temporal decay related to the coherence length of the probe laser pulses and (ii) the additional exponential temporal decay that could be potentially caused by unknown absorption of CAPs using the model signal $A\exp(-\alpha t)\exp[-2(t/\tau)^2]\cos(2\pi f_{B,\mathrm{LA}}t+\phi)$. Here, A is the amplitude, α the acoustic absorption coefficient, τ the coherence time of the probe laser pulses and ϕ the phase of the signal (see Supplementary information for details). The optical absorption of the probe green light was not considered because it is known to be negligible at the evaluated coherence length. The fit result demonstrated that the contribution of the acoustic absorption in the observed decay of the Brillouin amplitude is negligible too and that the decay of the TDBS signal in single crystals of ice is controlled by the coherence length because we obtained the fitted values of $L^{\mathrm{probe}}_{\mathrm{coherence}} \approx 13$ μm and $\tau_{\mathrm{probe}} \approx 125$ fs, consistent with the experimental pulse duration of the probe laser. Thus, the depth of imaging was limited in our experiments by the sample thickness. We note that application of lasers with pulses in ps-range, presently not commercially available for ASOPS although achievable from fs-lasers-based ASOPS systems with prisms or optical gratings, will allow a significant extension of the 3D-imaging depth of the TDBS-ASOPS method (not needed in our case) without any degradation of other imaging characteristics.

C. Comparison of the TDBS and X-ray imaging methods

As mentioned in the introduction, the most elaborated way to examine texture of polycrystalline solids, with the spatial resolution similar or better than the grain sizes, is X-ray microscopy. Yet, most of the techniques based on the X-ray CT provide only partial information related to sample texture or composition such as distinct absorption coefficients, refractive indices[6], or electron densities [*e.g.* in Ref. 48] of the constituting grains. For this reason, they are of limited interest for examination of texture of densified pore-free samples composed of light elements and/or of

only one compound. However, they permit examination of individual particles with a very high reconstruction resolution of < 0.1 µm. Similarly, coherent X-ray diffraction allows 3D imaging of morphology and strains in isolated deformed crystals with the reconstruction resolution of < 30 nm (e.g., Refs.[49,50]) as well as visualisation of twinning and dislocation dynamics in an individual nanoparticle using a particular Bragg reflection[50,51]. Yet, the particle itself and its position in the sample with respect to other particles (or a common system of coordinates) should be determined using another technique[51]. Dark field X-ray microscopy also permits 3D mapping, with the spatial resolution approaching 0.3 µm, of subgrains or even domains in individual particles having sizes around 10 µm[12,47,52]. Once again, the particle positions in the sample interior had to be determined using other techniques: either 3D X-ray Diffraction or Diffraction Contrast Tomography whose spatial reconstruction resolution was specified as 1 µm[12,47,52]. The differential-aperture X-ray microscopy provides 3D images without CT reconstruction with the resolution of ≤ 1 µm[53]. It requires, however, the rare polychromatic synchrotron X-ray microbeams to probe local crystal orientations and strains. Unfortunately, measurements for samples in devices with a limited access, *e.g.*, a DAC, were not yet published. In a polycrystalline pore-free sample, the latter techniques based on X-ray diffraction (XRD) are providing the most comprehensive 3D imaging of the position, shape and orientation of grains with respect to each other and/or with respect to a common coordinate system. Due to the nature of the XRD, these approaches permit distinguishing differently oriented particles of the same compound as well as particles of different phases of the same compound provided the particles are crystalline and their structures are known under the temperature and/or pressure conditions of the measurements.

While X-ray-based CT techniques are widely used for 3D imaging of polycrystalline solids, thorough discussions of quality and reliability of the 3D-images obtained with µm- or even sub-µm resolution are surprisingly underrepresented [*e.g.* Ref. 54]. The main source of uncertainties comes, obviously, from the procedure used to reconstruct a 3D image of a sample from the 2D projections collected upon its rotation. Here, the criteria applied to evaluate the image-reconstruction reliability, *e.g.* modulation transfer function, signal-to-noise ratio, or detection effectiveness, are of outstanding importance. A simple test of several X-ray-based 3D-scanners, consisting in determining the known ratio of microbeads of two monodisperse sizes of 10 µm and 20 µm, showed variations of almost one order of magnitude between the tested devices[54]. It was also reported that, by the use of the XRD-based CT and unhindered sample accessibility along two spatial directions, the reconstructed 3D-images exhibit "spotty" aspects as a consequence of the noncontinuous inten-

sity of the Debye–Scherrer rings[55]. The authors attributed this artifacts either to grain preferential orientations present in the examined cold-compressed sample or to large grain sizes relative to the beam size. Further difficulties can arise during *in-situ* measurements due to (i) use of intense focused X-ray beams altering the material texture or even melting caused by heating, (ii) incomplete solid-angle region accessible for X-rays when samples are located in tools or devices such as a DAC[56], a high-temperature oven or a cryostat, further aggravated by (iii) insufficient accuracy of displacement and rotation of such relatively heavy devices[12,54]. According to earlier works, the device/tool weight and an incomplete solid-angle region do not permit localization of grains with the accuracy better than 5-10 μm, thus strongly degrading the spatial resolution expected with X-ray-based imaging in more favorable experimental conditions[57–59]. Even when using the technically-primitive methods based on the X-ray absorption-contrast imaging (ACI) and phase-contrast imaging (PCI), the obtained 3D-images of entire samples, not to mention of grains inside the sample, did "not represent the absolute shape of the sample"[56].

Contrasting with the above-discussed limitations of X-ray methods, optical methods and especially the TDBS one, as demonstrated here, are better suited for getting local information directly from signals collected at a long-working distance and along a single direction: the rotation of relatively heavy devices are not needed anymore, partial access to samples is not an issue anymore. Providing that densities, refractive indices and single crystal elastic moduli of a tested (polycrystalline) sample are known from previous measurements, that could also involved TDBS measurements[27,28], the reconstruction of the 3D images from TDBS signals does require a minimal level of assumptions and could therefore be used for verification of the reliability of X-ray-based CT 3D imaging, at least where samples are located in devices with a limited access.

D. On the TDBS imaging with TA modes

Even though the TA modes showed up too sparsely to provide a qualitative 3D image as it has been done in Fig. 4 with the LA mode, the TA modes [Fig. 3(b)] are of a great importance and complementary to the LA mode because they allow identification of unknown grains and estimation of a set of possible crystallographic orientations of each recognized crystallite. The latter was done by scanning all propagation directions of the CAPs accompanied by the calculation of Brillouin frequencies of the corresponding LA and TA modes until they matched the measured Brillouin frequencies simultaneously. In some cases, the TA modes were the only way to distinguish two grains

having different orientations but the same LA velocity. Accordingly, the stronger the anisotropy of the TA modes, the stronger the contrast in the TA-mode-based images, which can even exceed that in LA-mode-based images and thus provides additional insight on the sample state[35]. So, in our measurement, the detection or not of a TA mode, together with the LA-mode-based 3D image, permitted identification of the H_2O-ice phase composing recognized grains.

For this aim, the below-described analysis of efficiency of generation of CAPs, and of each individual acoustic mode contributing to them, was performed. In TDBS measurements, generation of the LA and both TA modes in a sample (*e.g.* H_2O ice) occurs due to the mode conversion of the plane LA mode thermo-elastically generated in the isotropic optoacoustic transducer absorbing the pump laser pulses[60–62]. Thermo-elastic generation of CAPs directly in a transparent sample (*e.g.* H_2O ice) via heat transfer from the light absorbing transducer to the sample material is estimated to be negligible. If the interface between the optoacoustic transducer and the H_2O ice is flat and perfect, the elastic forces (stresses) and the mechanical displacements across the interface are continuous. In such case, the generation efficiency of each acoustic mode in the H_2O ice is directly proportional to the efficiency of the mode conversion, *i.e.*, transfer of the acoustic energy from the excited mode(s) in the transducer to each acoustic mode in the sample[60–62]. The transfer efficiency, depending on the particular orientation of each particular H_2O-ice crystallite relative to the interface, could be obtained by calculating the acoustic transmission coefficients, from an isotropic medium (the transducer) to an anisotropic medium (an arbitrary-oriented crystallite of the polycrystalline H_2O ice). We considered the particular case of a plane LA wave transmitted and mode-converted, at the interface, to a plane LA and two plane TA modes, respectively. Because the lateral size of the focused pump-laser spot was one order of magnitude larger than the probed acoustic wavelength, this transmission/conversion problem could be solved as one-dimensional where plane acoustic modes propagated normally through the interface. Changing relative orientation of the principal axis of an ice crystallite with respect to the normal to the interface we derived the transmission coefficients and thus the generation efficiency of each acoustic mode. Finally, to reveal reasons of a TA mode absence/presence in our TDBS signals, we assumed that detection of different acoustic modes predominantly takes place via the interaction of the probe light with the longitudinal, *i.e.*, the z strain component, of the acoustic modes. Details on the derivation of the generation efficiency can be found in Refs. 61 and 62, or else in any textbook dealing with the reflection and transmission coefficients of plane waves at an interface between two (anisotropic) solids[63,64].

Using the known mechanical properties of both phases of H_2O ice (Tab. I) and those of the cast iron (isotropic) reported to be $\rho_{Fe} = 7.87\ g\,cm^{-3}$, $C_{11}^{Fe} = 279$ GPa, and $C_{44}^{Fe} = 82$ GPa, the generation (transmission and mode conversion) efficiencies of each acoustic mode are calculated for both H_2O ice phases (Fig. 5). The efficiency values are plotted in Fig. 5 as a function of the orientation of the z-axis (the normal to the iron/ice interface, *i.e.*, the propagation direction) relative to the principal axes of ice crystals. The results are presented separately for different modes: for the LA mode in Figs. 5(a) and 5(d), for the FTA mode in Figs. 5(b) and 5(e), and for the STA mode in Figs. 5(c) and 5(f). For each acoustic mode transmitted in ice, with (TA) or without (LA) mode conversion, the transmission/mode conversion coefficient (Fig. 5) is defined as the ratio of the z strain component of the transmitted mode to the z strain component of the LA mode generated in iron and incident on the iron/ice interface. The results in Fig. 5 indicate that, for any crystallographic direction of any of the ice phases, the efficiency of generation of the LA mode is one-to-two orders of magnitude larger than for any of the two TA modes. We note also that the generation efficiency of the STA mode in phase VII is one order of magnitude larger than that of any other TA mode, which therefore partly explains why TA modes have not been observed for the phase VI and why mostly a single TA mode has been observed for the phase VII. According to our calculations, it is very probable that, in all grains of ice VII where only one TA mode was recognized, we dealt with the STA mode. As a result, a careful analysis of voxels with unidentified phases [copper colour scale in Fig. 3(a)] permitted attributing, with a high degree of confidence, the two center-bottom grains to the ice VII because the black dots denote the detection of TA modes in the related TDBS signals. In contrast, the top-left voxels in Fig. 3(a) are attributed to the ice VI because no TA modes could be recognized in the TDBS signals. This attribution is supported by the analysis of the whole xy cross-sections because the center-bottom grains are surrounded by the phase VII whereas the top-left one is surrounded by the phase VI.

Knowledge of the Brillouin frequencies of the LA modes permitted estimation of crystallographic directions of all recognized crystallites with respect to the CAP propagation direction and thus with respect to other crystallites in a common system of coordinates. Moreover, the crystallographic directions corresponding to the highest and the lowest LA-mode frequencies in crystals of each of the two phases could be recognized with the accuracy of the frequency measurement. For example, for the cubic phase VII of H_2O ice, the frequency of the LA mode along $\langle 111 \rangle$ is the highest while that along $\langle 100 \rangle$ is the lowest (e.g. Ref. 27). However, we were able to provide more detailed information on crystallographic orientations of particular crystallites if they showed

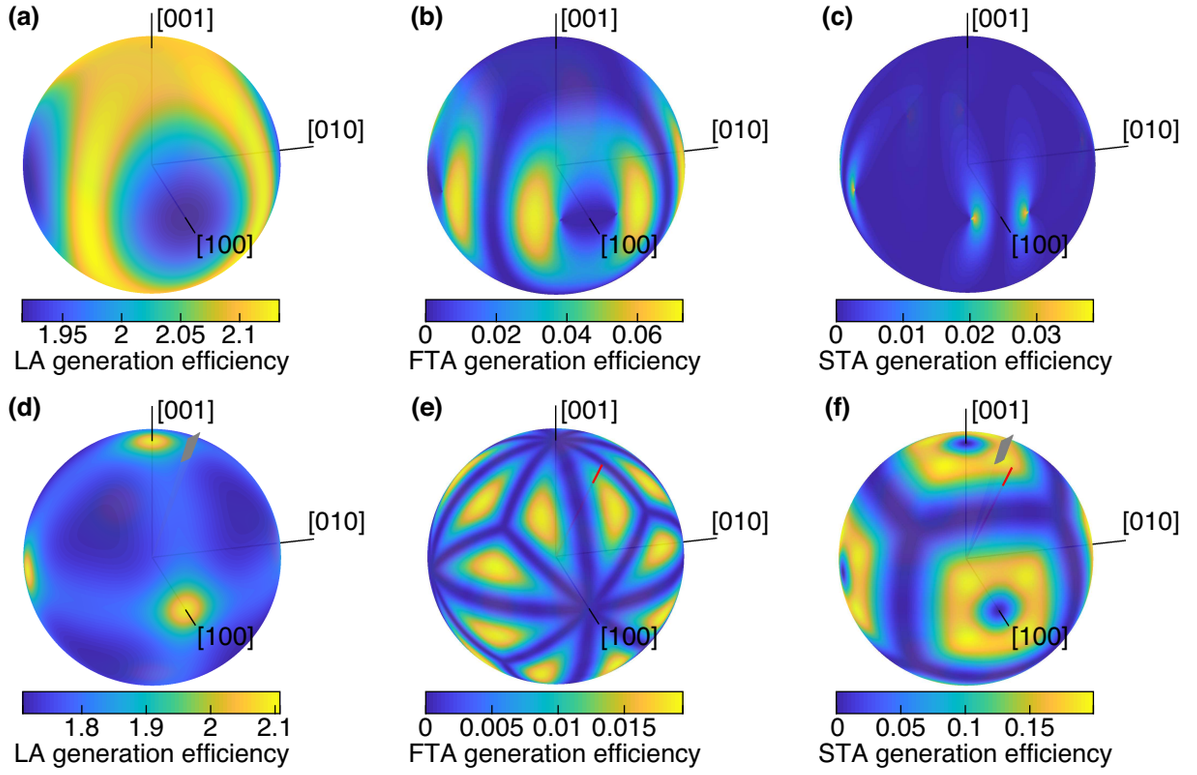

FIG. 5. Generation efficiency of each acoustic mode for (top) the phase VI and (bottom) the phase VII of H_2O ice along the principal axes of the crystals as a function of the orientation of the normal to the iron/ice interface relative to the ice crystal principal axes. The results are presented separately for different modes: in (a,d) for the LA mode, in (b,e) for the FTA mode, and in (c,f) for the STA mode.

both TA modes, in addition to the LA mode: For example, we consider such a crystallite of the phase VII located, in Fig. 2(b), at $x \approx 90$ µm and $y \approx 60$ µm. It was pointed out above that the dominant TA frequency was usually the lowest of the two TA modes, *i.e.*, the STA mode, which is consistent with our frequency calculations using the C_{ij}-values summarised in Table I. Knowing that in the considered crystallite the measured Brillouin frequencies are ~ 31.8 GHz, ~ 20.8 GHz, and ~ 15.4 GHz, the CAP propagation direction was found to form an angle φ of 17°-18° and an angle θ of 32°-33°, where φ and θ are the proper Euler angles of intrinsic rotations about moving axes e_Z-e'_X-e''_Z[65]. Of course, all symmetry-equivalent crystallographic directions are also possible. If we consider this direction in Fig. 5(e)-(f) (red thick line) then we recognize that it corresponds to a direction in which the FTA mode has a generation efficiency of about 0.01 (half of the highest possible efficiency) and that of the STA mode is of about 0.085, which explains the ease in the simultaneous detection of these two modes. If only one TA mode is measured, as in the centre of the sample occupied by the phase VII, it is likely that this mode is the slow one and the orientation of

the z-axis in the crystal principal axes is not unique anymore but defines a part of an arc ($\theta = 20°$, $\varphi \in [26°, 45°]$) shown in grey in Fig. 5(d,f). This is the case for the TDBS signal collected for the voxel with the coordinates $(x, y, z) = (50, 46.25, 1.25)$ µm in Fig. 2(b). As already mentioned above, detection of the LA mode alone, as is the case for the TDBS signals attributed to H_2O ice VI, permits only a rough estimation of orientations of the crystallites if the detected frequencies are not the extremes. However, detection of the LA mode and of one of the TA modes, whose type, *i.e.*, STA or FTA, is known (here from the analysis of the generation efficiency) allows bracketing the range of orientations to limits which could already be of interest for the comparison with micromechanical models describing behaviour of polycrystalline materials and their evolution upon external action, *e.g.*, nonhydrostatic compression. It is worth noting here that the determination of the propagation direction in a crystallite does not mean the complete orientation of the crystallite relative to other crystallites, because the crystallite could be arbitrary rotated around the z axis (interface normal). A complete orientation of crystallites could be obtained by performing TDBS measurements with different polarisations of the probe light[36], which will be a subject of the future work.

E. On the use of the detected TDBS signals with beatings

The above-mentioned observation of particular TDBS signals, corresponding to the simultaneous propagation of LA pulses in two adjacent crystallites [see black open squares in Fig. 3(a)] provides an original opportunity to localize the boundaries between them. If the interest is focused on imaging of grain boundaries, such signals can be used to 3D-map the boundaries and to follow their movement in real time while performing sample deformation. To do so, a feedback signal could indeed be designed out of the observation of beatings to control the displacement stage. This procedure will limit the number of measurement points and thus accelerate the imaging procedure of grain boundaries drastically.

F. On the data collection rate

Last but not least, the here-presented 3D image was collected during 110 hours because we kept powers of both lasers very low (below 10 mW). However, the image collection can be accelerated by 2 orders of magnitude, if both lasers are used at the full power of $\sim$ 100 mW. The low laser

powers were used in order to exclude possible progress of the transition from ice VII to ice VI observed to occur when one spot in the sample is illuminated for long time[41]. We remind, that this phase transition is not initiated by thermal heating (the estimated stationary and transient temperature rises did not exceed 3 °C) but by electrons photo-generated in the conduction band of diamond[41]. Because our 3D image (Fig. 4) contains about 58500 voxels (lateral step of 1.2 µm and axial of $\sim$ 1.2 µm), we estimated the data collection rate of the presented TDBS-ASOPS measurement to be $\sim$ 0.15 voxel/s. If the 3D imaging is performed on a sample containing only one phase and far from the phase transition boundary, the full laser powers can be used and the duration of collection of a similar 3D image will drop to $\sim$ 65 minutes, which corresponds to the data collection rate of $\sim$ 15 voxel/s. For comparison, an XRD-based CT examination (at the ESRF, one of the most powerful synchrotron radiation sources) of a sample with lateral and axial sizes of $\sim$ 1 mm and the spatial resolution of $\sim$ 27 µm ($\sim$ 32000 voxels) required 8 hours (or $\sim$ 1 voxel/s) but the obtained 3D image still contained artefacts[55]. According to the authors of this work, the artefacts were caused by orientational texture and big grain sizes of the examined material. Such effect makes the XRD-based CT less suitable for the 3D-imaging of texture of polycrystalline solids, one of the main purposes of such imaging measurements. The artefacts caused by a sample texture are not possible in 3D-images obtained using the TDBS-ASOPS technique because the signals are collected directly from each voxel and the data treatment is nearly free of assumption. High laser powers can be used for examination of condensed matter in a DAC because the samples inside are thin and the diamond anvils are a very efficient heat sink, especially when pressure increases in the Mbar range and above. Despite of the immense pressure difference from 2 GPa to 100 GPa, both lateral and axial resolution of the TDBS-ASOPS technique does not degrade[12,27,28]. The higher pump and probe laser powers result then in stronger TDBS signals and thus a more efficient detection of TA modes in the Mbar range promising a more detailed 3D-imaging of texture of transparent polycrystalline samples at extreme conditions of high pressures and, eventually, high-temperatures to several thousands °C if combined with laser heating (e.g. Ref. 66). We emphasize that a DAC is only one example of devices with a limited access. It can be extended to cryostats, very high-temperature ovens (well above 1000 °C), and reactors of different types.

V. CONCLUSIONS

We reported on advances in applications of the time-domain Brillouin scattering (TDBS) technique for 3D imaging of transparent polycrystalline samples located in a device with a limited access, along only one spatial direction and from one side only. The applied TDBS-ASOPS set-up provided a comprehensive, reliable high-resolution *in-situ* 3D visualisation of microstructure of a transparent polycrystalline sample of H_2O ice compressed in a diamond anvil cell (DAC) to 2.15 GPa where two phases, ice VI and ice VII, coexist. The approach permits, in general, 3D images of samples with infinite lateral sizes and thicknesses of at least 10 μm in their entirety. The latter means that the TDBS-ASOPS provides shapes and relative coordinates of all grains (if resolved) with respect to each other or a common coordinate system, independent of their phase composition with, in our experiments, the lateral resolution of 2.5 μm and the axial one of 1.2 μm, identification of phase of each particular grain, as well as crystallographic orientation of the identified grains with respect to a common coordinate system. The here-reported resolution of the TDBS-ASOPS technique can be further improved down to the optical diffraction limit in the lateral direction, say down to 150 nm, if a blue-UV probe laser is used and the sample is transparent for these wavelengths, and to sub-optical dimension in the axial direction, theoretically down to the nanometers length of the coherent acoustic pulse or of the strain front in it[16]. The 3D images, obtained using the TDBS technique, are reliable because the information is recovered directly for each image voxel using minimal level of assumptions. Accuracy of the recovered information (*e.g.*, crystallite orientations) depends only on the quality and content of the TDBS signals and the degree of elastic anisotropy of the examined crystalline material that can be measured in advance using the same technique (see Refs. 27 and 28).

In the here-presented 3D imaging experiments, we observed, for the first time at high pressures in a DAC, TDBS signals containing contribution of quasi-shear coherent acoustic pulses (CAPs). We demonstrated some examples of fruitful application of the TDBS imaging with several acoustic modes simultaneously. We revealed the possibility to localize positions of grain boundaries in a transparent polycrystal by the identification of specific TDBS signals that are due to the simultaneous propagation of an acoustic pulse in two adjacent grains. Overall, our reported results are a big step towards the perspective of full 3D characterization of sample texture at extreme conditions (high pressures and/or temperatures) and its evolution on further compression, temperature change or any other type of action. Such characterization is of special interest for different branches of

research at extreme conditions. It will make possible *in-situ* examination of texture of minerals present in the deep Earth and its evolution upon nonhydrostatic compression with the detailedness presently not accessible by other techniques. Such information will permit conclusion about the nature of seismic anisotropies observed in the Earth's mantle. Also, it could help to quantitatively investigate (i) kinetics of phase transitions and chemical reactions at high pressures and/or high or low temperatures as well as (ii) relations between the crystallographic orientations of crystallites of the forming phase and of those of the parent phase. Obviously, further improvement of the signal treatment and resolution of the 3D TDBS imaging permitting recovery of quantitative values of shear sound velocities in the same time as longitudinal sound velocities and within the full imaged volume will further extend the horizons of investigation of solids at extreme conditions. We believe that 3D images collected using the TDBS-ASOPS technique can be used for the verification of 3D images obtained using the X-ray-based CT, especially for samples located in devices with a limited access.

SUPPLEMENTARY MATERIAL

See supplementary material for the details about the distribution of the Brillouin frequency for phases VI and VII of H_2O ice, the detailed discussion on the coherence length of the probe laser pulses, and the micro-Raman spectrometry of the water ice sample.

ACKNOWLEDGEMENTS

This work was supported by the French National Research Agency (ANR, France) through the grant <ANR-18-CE42-0017>. T.T. was supported by the Région Pays de la Loire through the RFI Le Mans Acoustique (project "Paris Scientifique OPACOP 2018"). E.D.L.S. was supported by the program Acoustic Hub® funded by the Région Pays de la Loire. We thank our colleagues from NETA who provided insight and expertise that greatly assisted the research.

DATA AVAILABILITY

The data that support the findings of this study are available from the corresponding author upon reasonable request.

APPENDIX: ESTIMATION OF THE EXPECTED BRILLOUIN FREQUENCIES IN BOTH PHASES VI AND VII OF WATER ICE AT 2.15 GPa

At the room temperature and the pressure of 2.15 GPa, both phases VI and VII of H_2O ice are coexisting (phase transition)[43,44,67–69]. We give here details on the way the Brillouin frequencies have been estimated for both phases. The goal was to have at hand estimated values of the expected Brillouin frequencies for the subsequent analysis of the experimental data. The error of the estimates is overall not very small, especially because of the drastic change of properties the sample material can exhibit at the phase transition. We do believe though that the below presented strategy of extrapolation allows the 3D characterization of individual ice grains at high-pressure and in two-phase region with an acceptable correctness.

The densities, reported in the first row of Tab. I, are deduced by interpolating the same data than the ones used in Fig. 3 of Ref. 43 plotting the density of the various H_2O forms as a function of pressure. Uncertainties in the densities in Ref. 43 (also used in Ref. 44, wherefrom the elastic constants were taken) are negligible in comparison with uncertainties of the elastic moduli. The elastic constants are deduced by fitting and extrapolating to a pressure of 2.15 GPa the results presented in Figs. 4 and 5 of Ref. 44. Thus, the accuracy of $\sim \pm 2\%$, reported in Ref. 44 for the ratios of the elastic moduli and the density, results in $\sim \pm 2\%$ accuracy in the moduli and in $\sim \pm 1\%$ accuracy in velocities of the acoustic modes[44]. The refractive index of ice was evaluated in Ref. 44 (Fig. 3) with the accuracy of $\sim \pm 2\%$.

To calculate the Brillouin frequency ranges, the density and the elastic constants are used to solve the Christoffel equation for all possible propagation directions to get the minimal and maximal possible velocities for each acoustic mode in each phase of H_2O ice. Then Eq. (1) is used to get the minimal and maximal possible Brillouin frequencies in each case. Since the acoustic velocities are known in any propagation direction of the CAPs, so do the Brillouin frequencies. Combining the uncertainties in velocities and in the refractive indices, we could conclude that maximal and minimal Brillouin frequencies in Table I and Fig. S1 (see Supplementary information) are determined with the uncertainties of $\sim \pm 3\%$. The uncertainty of the Brillouin frequencies confining the overlap interval of the LA Brillouin frequencies in ices VI and VII, *i.e.* $[27.5, 29.4]$ GHz, can be scaled respectively. Thus, the overlap interval shrinks but does not disappear ($[27.5, 29.4]$ GHz $\Rightarrow [28.3, 28.5]$ GHz).

AUTHOR CONTRIBUTIONS STATEMENT

A.Z.,V.E.G., S.R., N.C. and A.B. designed the research, N.C. and A.Z. prepared the sample, S.S., E.D.L.S, S.R., N.C. and A.B contributed to the experiments, S.R., T.T., S.S., E.D.L.S and V.T. contributed to signal processing, V.E.G., S.R., T.T. ans S.S. developed the theoretical estimates, S.R., V.E.G., A.Z., S.S., N.C., A.B. and V.T. analysed and interpreted the experimental observations, S.R., V.E.G. and A.Z. wrote the manuscript. All authors reviewed the manuscript.

ADDITIONAL INFORMATION

The authors declare no competing interests.

REFERENCES

[1]T. M. Heenan, C. Tan, J. Hack, D. J. Brett, and P. R. Shearing, "Developments in X-ray tomography characterization for electrochemical devices," Materials Today **31**, 69 – 85 (2019).

[2]M. Kodur, R. E. Kumar, Y. Luo, D. N. Cakan, X. Li, M. Stuckelberger, and D. P. Fenning, "X-ray microscopy of halide perovskites: Techniques, applications, and prospects," Advanced Energy Materials **10**, 1903170 (2020).

[3]D. Faulkner, C. Jackson, R. Lunn, R. Schlische, Z. Shipton, C. Wibberley, and M. Withjack, "A review of recent developments concerning the structure, mechanics and fluid flow properties of fault zones," Journal of Structural Geology **32**, 1557 – 1575 (2010).

[4]K. V. Falch, D. Casari, M. Di Michiel, C. Detlefs, A. Snigireva, I. Snigireva, V. Honkimäki, and R. H. Mathiesen, "In situ hard X-ray transmission microscopy for material science," Journal of Materials Science **52**, 3497–3507 (2017).

[5]S. Matsuyama, K. Maeshima, and M. Shimura, "Development of X-ray imaging of intracellular elements and structure," Journal of Analytical Atomic Spectrometry **35**, 1279–1294 (2020).

[6]M. Endrizzi, "X-ray phase-contrast imaging," Nuclear Instruments and Methods in Physics Research Section A:

[7]W. A. Bassett, "Diamond anvil cell, 50th birthday," High Pressure Research **29**, 163–186 (2009).

[8]M. I. Eremets, *High pressure experimental methods*, Oxford science publications (Oxford University, Oxford ; New York, 1996).

[9]A. Jayaraman, "Diamond anvil cell and high-pressure physical investigations," Reviews of Modern Physics **55**, 65–108 (1983).

[10]G. Scarcelli and S. H. Yun, "Confocal Brillouin microscopy for three-dimensional mechanical imaging," Nature Photonics **2**, 39–43 (2008).

[11]G. Scarcelli, W. J. Polacheck, H. T. Nia, K. Patel, A. J. Grodzinsky, R. D. Kamm, and S. H. Yun, "Noncontact three-dimensional mapping of intracellular hydromechanical properties by Brillouin microscopy," Nature Methods **12**, 1132–1134 (2015).

[12]S. M. Nikitin, N. Chigarev, V. Tournat, A. Bulou, D. Gasteau, B. Castagnede, A. Zerr, and V. E. Gusev, "Revealing sub-μm and μm-scale textures in H_2O ice at megabar pressures by time-domain Brillouin scattering," Scientific Reports **5**, 9352 (2015).

[13]G. Antonacci, V. de Turris, A. Rosa, and G. Ruocco, "Background-deflection brillouin microscopy reveals altered biomechanics of intracellular stress granules by als protein fus," Communications Biology **1**, 139 (2018).

[14]C. Thomsen, H. Grahn, H. Maris, and J. Tauc, "Picosecond interferometric technique for study of phonons in the brillouin frequency range," Optics Communications **60**, 55–58 (1986).

[15]H. Grahn, H. Maris, and J. Tauc, "Picosecond ultrasonics," IEEE Journal of Quantum Electronics **25**, 2562–2569 (1989).

[16]V. E. Gusev and P. Ruello, "Advances in applications of time-domain Brillouin scattering for nanoscale imaging," Applied Physics Reviews **5**, 031101 (2018).

[17]S. A. Akhmanov and V. E. Gusev, "Laser excitation of ultrashort acoustic pulses: New possibilities in solid-state spectroscopy, diagnostics of fast processes, and nonlinear acoustics," Soviet Physics Uspekhi **35**, 153–191 (1992).

[18]P. Ruello and V. E. Gusev, "Physical mechanisms of coherent acoustic phonons generation by ultrafast laser action," Ultrasonics **56**, 21–35 (2015).

[19]I. L. Fabelinskii, *Molecular Scattering of Light* (Springer New York, Boston, MA, 1968).

[20]J. G. Dil, "Brillouin scattering in condensed matter," Reports on Progress in Physics **45**, 285–334 (1982).

[21]A. Steigerwald, Y. Xu, J. Qi, J. Gregory, X. Liu, J. K. Furdyna, K. Varga, A. B. Hmelo, G. Lüpke, L. C. Feldman, and N. Tolk, "Semiconductor point defect concentration profiles measured using coherent acoustic phonon waves," Applied Physics Letters **94**, 111910 (2009).

[22]C. Mechri, P. Ruello, J. M. Breteau, M. R. Baklanov, P. Verdonck, and V. Gusev, "Depth-profiling of elastic inhomogeneities in transparent nanoporous low-k materials by picosecond ultrasonic interferometry," Applied Physics Letters **95**, 091907 (2009).

[23]A. M. Lomonosov, A. Ayouch, P. Ruello, G. Vaudel, M. R. Baklanov, P. Verdonck, L. Zhao, and V. E. Gusev, "Nanoscale Noncontact Subsurface Investigations of Mechanical and Optical Properties of Nanoporous Low-*k* Material Thin Film," ACS Nano **6**, 1410–1415 (2012).

[24]F. Decremps, L. Belliard, B. Perrin, and M. Gauthier, "Sound Velocity and Absorption Measurements under High Pressure Using Picosecond Ultrasonics in a Diamond Anvil Cell: Application to the Stability Study of AlPdMn," Physical Review Letters **100**, 035502 (2008).

[25]M. R. Armstrong, J. C. Crowhurst, E. J. Reed, and J. M. Zaug, "Ultrafast high strain rate acoustic wave measurements at high static pressure in a diamond anvil cell," Applied Physics Letters **92**, 101930 (2008).

[26]M. Kuriakose, S. Raetz, N. Chigarev, S. M. Nikitin, A. Bulou, D. Gasteau, V. Tournat, B. Castagnede, A. Zerr, and V. E. Gusev, "Picosecond laser ultrasonics for imaging of transparent polycrystalline materials compressed to megabar pressures," Ultrasonics **69**, 259–267 (2016).

[27]M. Kuriakose, S. Raetz, Q. M. Hu, S. M. Nikitin, N. Chigarev, V. Tournat, A. Bulou, A. Lomonosov, P. Djemia, V. E. Gusev, and A. Zerr, "Longitudinal sound velocities, elastic anisotropy, and phase transition of high-pressure cubic H_2O ice to 82 GPa," Physical Review B **96**, 134122 (2017).

[28]S. Raetz, M. Kuriakose, P. Djemia, S. M. Nikitin, N. Chigarev, V. Tournat, A. Bulou, A. Lomonosov, V. E. Gusev, and A. Zerr, "Elastic anisotropy and single-crystal moduli of solid argon up to 64 GPa from time-domain Brillouin scattering," Physical Review B **99**, 224102 (2019).

[29]S. Danworaphong, M. Tomoda, Y. Matsumoto, O. Matsuda, T. Ohashi, H. Watanabe, M. Nagayama, K. Gohara, P. H. Otsuka, and O. B. Wright, "Three-dimensional imaging of biological cells with picosecond ultrasonics," Applied Physics Letters **106**, 163701 (2015).

[30]F. Pérez-Cota, R. J. Smith, E. Moradi, L. Marques, K. F. Webb, and M. Clark, "Thin-film optoacoustic transducers for subcellular Brillouin oscillation imaging of individual biological cells," Applied Optics **54**, 8388 (2015).

[31]F. Pérez-Cota, R. J. Smith, E. Moradi, L. Marques, K. F. Webb, and M. Clark, "High resolution 3D imaging of living cells with sub-optical wavelength phonons," Scientific Reports **6**, 39326 (2016).

[32]M. Lejman, G. Vaudel, I. C. Infante, P. Gemeiner, V. E. Gusev, B. Dkhil, and P. Ruello, "Giant ultrafast photo-induced shear strain in ferroelectric $BiFeO_3$,"

Nature Communications **5**, 4301 (2014).

[33]M. Lejman, G. Vaudel, I. C. Infante, I. Chaban, T. Pezeril, M. Edely, G. F. Nataf, M. Guennou, J. Kreisel, V. E. Gusev, B. Dkhil, and P. Ruello, "Ultrafast acousto-optic mode conversion in optically birefringent ferroelectrics," Nature Communications **7**, 12345 (2016).

[34]M. Khafizov, J. Pakarinen, L. He, H. Henderson, M. Manuel, A. Nelson, B. Jaques, D. Butt, and D. Hurley, "Subsurface imaging of grain microstructure using picosecond ultrasonics," Acta Materialia **112**, 209–215 (2016).

[35]Y. Wang, D. H. Hurley, Z. Hua, G. Sha, S. Raetz, V. E. Gusev, and M. Khafizov, "Nondestructive characterization of polycrystalline 3D microstructure with time-domain Brillouin scattering," Scripta Materialia **166**, 34–38 (2019).

[36]Y. Wang, D. H. Hurley, Z. Hua, T. Pezeril, S. Raetz, V. E. Gusev, V. Tournat, and M. Khafizov, "Imaging grain microstructure in a model ceramic energy material with optically generated coherent acoustic phonons," Nature Communications **11**, 1597 (2020).

[37]L. Merrill and W. A. Bassett, "Miniature diamond anvil pressure cell for single crystal x-ray diffraction studies," Review of Scientific Instruments **45**, 290–294 (1974).

[38]H. K. Mao, J. Xu, and P. M. Bell, "Calibration of the ruby pressure gauge to 800 kbar under quasi-hydrostatic conditions," Journal of Geophysical Research: Solid Earth **91**, 4673–4676 (1986).

[39]S. Dilhaire, W. Claeys, J.-M. Rampnoux, and C. Rossignol, "Optical heterodyne sampling device having probe and pump beams," (2010), u.S. Patent US 007728317 B2.

[40]A. Bartels, R. Cerna, C. Kistner, A. Thoma, F. Hudert, C. Janke, and T. Dekorsy, "Ultrafast time-domain spectroscopy based on high-speed asynchronous optical sampling," Review of Scientific Instruments **78**, 035107 (2007).

[41]M. Kuriakose, N. Chigarev, S. Raetz, A. Bulou, V. Tournat, A. Zerr, and V. E. Gusev, "*In situ* imaging of the dynamics of photo-induced structural phase transition at high pressures by picosecond acoustic interferometry," New Journal of Physics **19**, 053026 (2017).

[42]"Filtering and smoothing data: Local regression smoothing. Copyright 2001-2016 The MathWorks, Inc. `https://mathworks.com/help/curvefit/smoothing-data.html`," (2020).

[43]A. Polian and M. Grimsditch, "Brillouin scattering from H_2O: Liquid, ice VI, and ice VII," Physical Review B **27**, 6409–6412 (1983).

[44]H. Shimizu, T. Nabetani, T. Nishiba, and S. Sasaki, "High-pressure elastic properties of the VI and VII phase of ice in dense H_2O and D_2O," Physical Review B **53**, 6107–6110 (1996).

[45]A. Devos and R. Côte, "Strong oscillations detected by picosecond ultrasonics in silicon: Evidence for an electronic-structure effect," Physical Review B **70**, 125208 (2004).

[46]A. Devos, R. Côte, G. Caruyer, and A. Lefèvre, "A different way of performing picosecond ultrasonic measurements in thin transparent films based on laser-wavelength effects," Applied Physics Letters **86**, 211903 (2005).

[47]H. Simons, A. King, W. Ludwig, C. Detlefs, W. Pantleon, S. Schmidt, F. Stöhr, I. Snigireva, A. Snigirev, and H. F. Poulsen, "Dark-field X-ray microscopy for multiscale structural characterization," Nature Communications **6**, 6098 (2015).

[48]E. H. R. Tsai, J. Billaud, D. F. Sanchez, J. Ihli, M. Odstrčil, M. Holler, D. Grolimund, C. Villevieille, and M. Guizar-Sicairos, "Correlated X-ray 3D ptychography and diffraction microscopy visualize links between morphology and crystal structure of lithium-rich cathode materials," *iScience*, iScience **11**, 356–365 (2019).

[49]X. Huang, W. Yang, R. Harder, Y. Sun, M. Lu, Y. S. Chu, I. K. Robinson, and H.-k. Mao, "Deformation twinning of a silver nanocrystal under high pressure," *Nano Letters*, Nano Letters **15**, 7644–7649 (2015).

[50]H.-K. Mao, B. Chen, J. Chen, K. Li, J.-F. Lin, W. Yang, and H. Zheng, "Recent advances in high-pressure science and technology," Matter and Radiation at Extremes **1**, 59–75 (2016).

[51]A. Ulvestad, A. Singer, J. N. Clark, H. M. Cho, J. W. Kim, R. Harder, J. Maser, Y. S. Meng, and O. G. Shpyrko, "Topological defect dynamics in operando battery nanoparticles," Science **348**, 1344–1347 (2015).

[52]P. Reischig, A. King, L. Nervo, N. Viganó, Y. Guilhem, W. J. Palenstijn, K. J. Batenburg, M. Preuss, and W. Ludwig, "Advances in X-ray diffraction contrast tomography: flexibility in the setup geometry and application to multiphase materials," Journal of Applied Crystallography **46**, 297–311 (2013).

[53]B. C. Larson, W. Yang, G. E. Ice, J. D. Budai, and J. Z. Tischler, "Three-dimensional X-ray structural microscopy with submicrometre resolution," Nature **415**, 887–890 (2002).

[54]S. Zabler, M. Ullherr, C. Fella, R. Schielein, O. Focke, B. Zeller-Plumhoff, P. Lhuissier, W. DeBoever, and R. Hanke, "Comparing image quality in phase contrast subμ X-ray tomography—A round-robin study," Nuclear Instruments and Methods in Physics Research Section A: Accelerators, Spectrometers, Detectors and A

[55]M. Álvarez-Murga, J. P. Perrillat, Y. Le Godec, F. Bergame, J. Philippe, A. King, N. Guignot, M. Mezouar, and J. L. Hodeau, "Development of synchrotron X-ray micro-tomography under extreme conditions of pressure and temperature," Journal of Synchrotron Radiation **24**, 240–247 (2017).

[56]K. Ohta, T. Wakamatsu, M. Kodama, K. Kawamura, and S. Hirai, "Laboratory-based x-ray computed tomography for 3d imaging of samples in a diamond anvil cell in situ at high pressures," Review of Scientific Instruments **91**, 093703 (2020).

[57]C. Nisr, G. Ribárik, T. Ungár, G. B. M. Vaughan, P. Cordier, and S. Merkel, "High resolution three-dimensional X-ray diffraction study of dislocations in grains of $MgGeO_3$ post-perovskite at 90 GPa," Journal of Geophysical Research: Solid Earth **117**, B03201 (2012).

[58]C. Nisr, G. Ribárik, T. Ungár, G. B. Vaughan, and S. Merkel, "Three-dimensional X-ray diffraction in the diamond anvil cell: application to stishovite," High Pressure Research **34**, 158–166 (2014).

[59]G. E. Ice, P. Dera, W. Liu, and H.-k. Mao, "Adapting polychromatic X-ray microdiffraction techniques to high-pressure research: energy scan approach," Journal of Synchrotron Radiation **12**, 608–617 (2005).

[60]T. Bienville and B. Perrin, "Generation and detection of quasi transverse waves in an anisotropic crystal by picosecond ultrasonics," in *Proceedings of the WCU 2003, Paris* (2003) pp. 813–816.

[61]T. Pezeril, P. Ruello, S. Gougeon, N. Chigarev, D. Mounier, J.-M. Breteau, P. Picart, and V. Gusev, "Generation and detection of plane coherent shear picosecond acoustic pulses by lasers: Experiment and theory," Physical Review B **75**, 174307 (2007).

[62]Y. Wang and M. Khafizov, "Shear wave generation by mode conversion in picosecond ultrasonics: Impact of grain orientation and material properties," Journal of the American Ceramic Society **104**, 2788–2798 (2021).

[63]B. Auld, "Acoustic fields and waves in solids," (R. E. Krierger Publishing Compagny, Malabar, Florida, 1990) Chap. 9. Reflection and Refraction (9-E. Anisotropic Fresnel equations), pp. 38–57.

[64]D. Royer and E. Dieulesaint, "Elastic waves in solids," (Masson, Paris, 1999) Chap. 4. Plane Waves in Crystals (4-4. Reflection and refraction), pp. 229–248.

[65]G. Nolze, "Euler angles and crystal symmetry," Crystal Research and Technology **50**, 188–201 (2015).

[66]A. Zerr, G. Serghiou, and R. Boehler, "Phase transitions and material synthesis using the CO2-laser heating technique in a diamond cell," in

938 *Handbook of ceramic hard materials. Hrsg.: R. Riedel. - Weinheim: Wiley-VCH, 2000. S. 41-65*,
939 edited by R. Riedel (Wiley-VCH, Weinheim, 2000).
940 [67]H. Shimizu, "Elastic properties of dense H_2O-ices studied by brillouin spectroscopy,"
941 Physica B: Condensed Matter **219-220**, 559 – 561 (1996).
942 [68]B. J. Baer, J. M. Brown, J. M. Zaug, D. Schiferl, and E. L. Chronister, "Impulsive stimulated
943 scattering in ice vi and ice vii," The Journal of Chemical Physics **108**, 4540–4544 (1998).
944 [69]A. N. Dunaeva, D. V. Antsyshkin, and O. L. Kuskov, "Phase diagram of
945 H_2O: Thermodynamic functions of the phase transitions of high-pressure ices,"
946 Solar System Research **44**, 202–222 (2010).

LIST OF FIGURES

LIST OF TABLES

Journal of Applied Physics

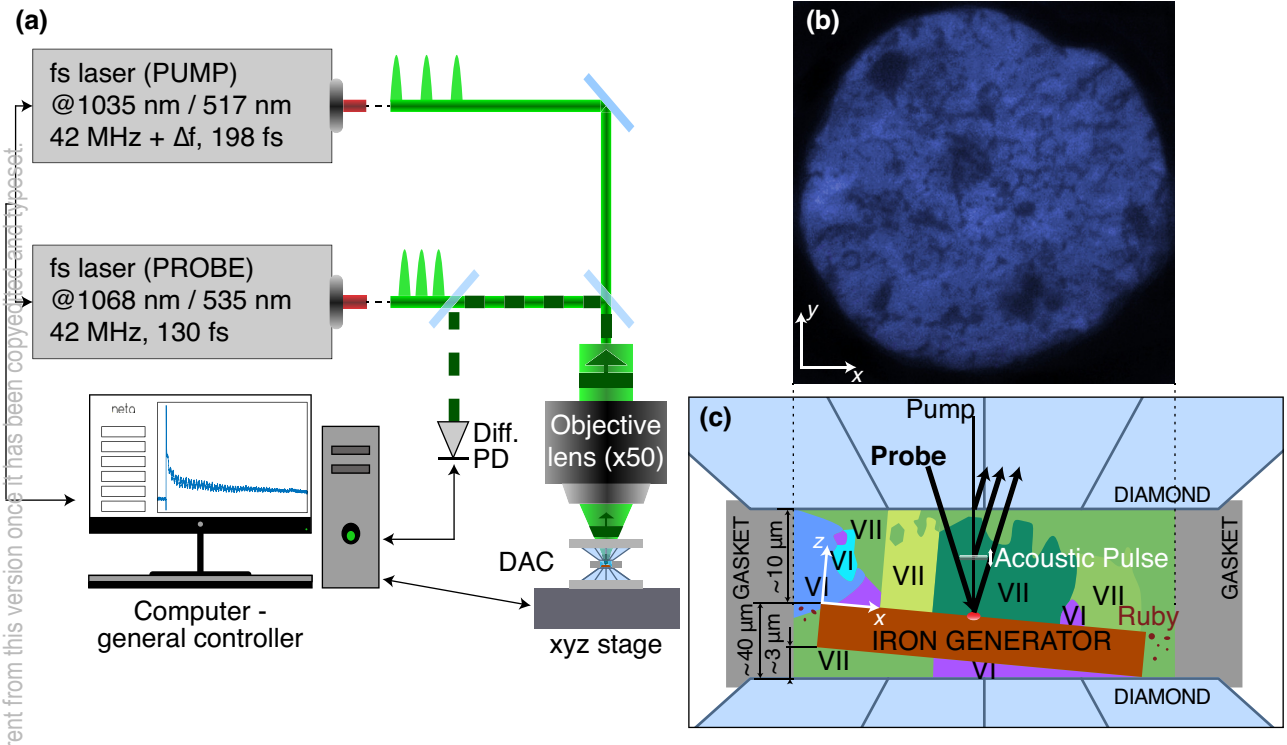

Journal of Applied Physics

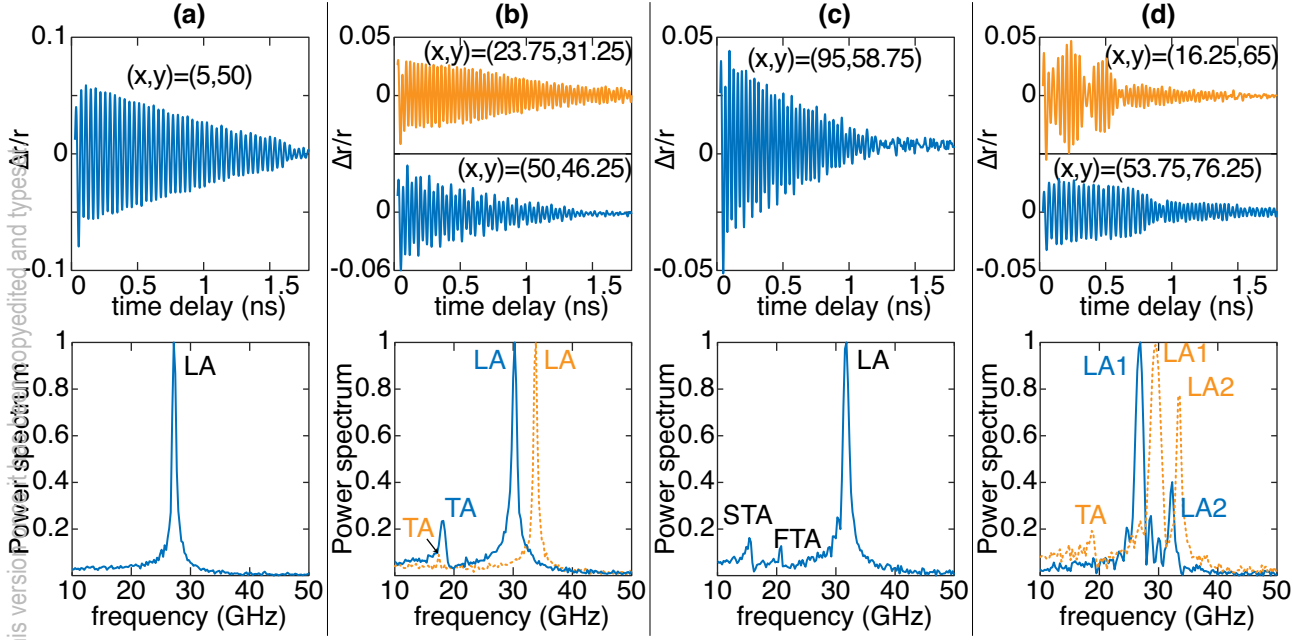

Journal of Applied Physics

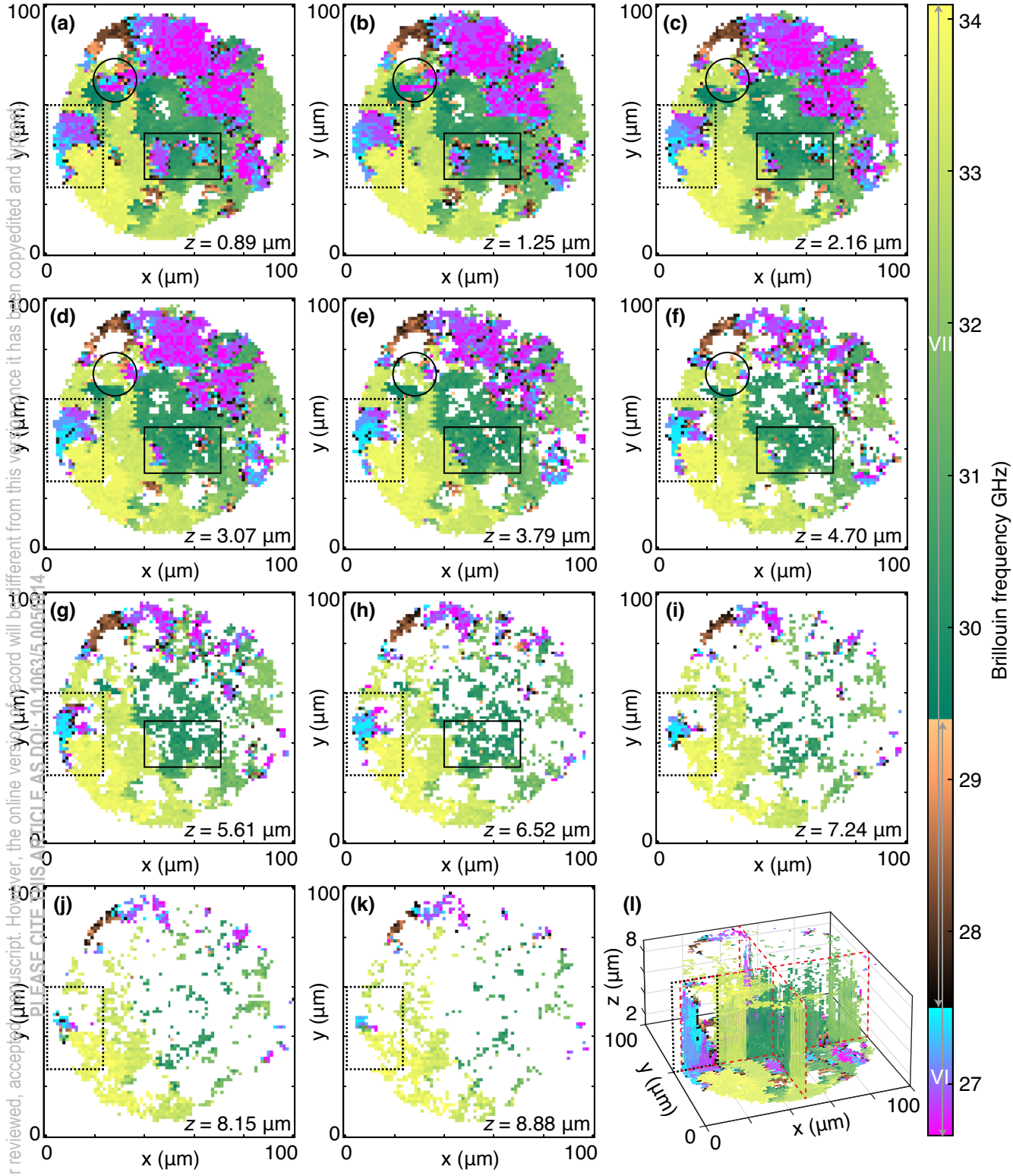

Journal of Applied Physics